Twentieth-Century Climate Change over Africa: Seasonal Hydroclimate Trends and Sahara Desert Expansion

NATALIE THOMAS AND SUMANT NIGAM[a]

Department of Atmospheric and Oceanic Science, University of Maryland, College Park, College Park, Maryland

(Manuscript received 21 March 2017, in final form 9 November 2017)

ABSTRACT

Twentieth-century trends in seasonal temperature and precipitation over the African continent are analyzed from observational datasets and historical climate simulations. Given the agricultural economy of the continent, a seasonal perspective is adopted as it is more pertinent than an annual-average one, which can mask offsetting but agriculturally sensitive seasonal hydroclimate variations. Examination of linear trends in seasonal surface air temperature (SAT) shows that heat stress has increased in several regions, including Sudan and northern Africa where the largest SAT trends occur in the warm season. Broadly speaking, the northern continent has warmed more than the southern one in all seasons. Precipitation trends are varied but notable declining trends are found in the countries along the Gulf of Guinea, especially in the source region of the Niger River in West Africa, and in the Congo River basin. Rainfall over the African Great Lakes—one of the largest freshwater repositories—has, however, increased. It is shown that the Sahara Desert has expanded significantly over the twentieth century, by 11%–18% depending on the season, and by 10% when defined using annual rainfall. The expansion rate is sensitively dependent on the analysis period in view of the multidecadal periods of desert expansion (including from the drying of the Sahel in the 1950s–80s) and contraction in the 1902–2013 record, and the stability of the rain gauge network. The desert expanded southward in summer, reflecting retreat of the northern edge of the Sahel rainfall belt, and to the north in winter, indicating potential impact of the widening of the tropics. Specific mechanisms for the expansion are investigated. Finally, this observational analysis is used to evaluate the state-of-the-art climate simulations from a comparison of the twentieth-century hydroclimate trends. The evaluation shows that modeling regional hydroclimate change over the African continent remains challenging, warranting caution in the development of adaptation and mitigation strategies.

1. Introduction

Climate change has footprints across the planet; however, certain regions are disproportionately affected. Africa is less responsible for the occurrence of anthropogenic climate change than any other continent (Fields 2005) but more vulnerable to its effects on account of its high population, low adaptive capacity, and multiple converging stressors (Busby et al. 2014; Fields 2005; Niang et al. 2014). Africa is furthermore an interesting case study for climate change due to its unique climatological features. It is the only continent that has almost equal parts in the Southern and Northern Hemispheres (Collins 2011) and thus is home to a wide variety of climate zones. It consists of the Sahara Desert and Sahel in northern Africa, the Namib–Kalahari Desert in southern Africa, tropical rain forest in equatorial Africa, and grasslands and savanna in between. The prevalence of land surface effects, internal climate variability, and sensitivity to global sea surface temperatures make the continent climatically complex (Hulme et al. 2001).

Several studies have investigated the trends in precipitation and surface air temperature over the continent. Precipitation variability occurs on a range of climate time scales; low-frequency variability, characteristic of West Africa and the Sahel, is associated with multidecadal changes in sea surface temperature (SST) and atmospheric circulation (e.g., Nicholson 2001; Zhang and Delworth 2006; Nigam and Ruiz-Barradas 2016) whereas higher-frequency variability, seen in

[a] Additional affiliation: Jefferson Science Fellow, The National Academy of Sciences, Engineering and Medicine, Washington, D.C.

Corresponding author: Sumant Nigam, nigam@umd.edu

DOI: 10.1175/JCLI-D-17-0187.1

eastern and southern Africa (e.g., Nicholson and Kim 1997; Schreck and Semazzi 2004), is connected to El Niño–Southern Oscillation (ENSO; Philander 1990) and other subdecadal processes (e.g., Hulme et al. 2001; Nicholson 2001; Omondi et al. 2013).

Precipitation trends have been particularly well studied over the Sahel region. The drying trends have been related to land surface processes, including amplification of meteorological drought from biophysical (Charney 1975) and surface hydrologic feedbacks (Nicholson 2000). Regional and global patterns of SST anomalies have also been implicated (Folland et al. 1986; Giannini et al. 2003) as have sulfate aerosols in the Northern Hemisphere through their effect on Atlantic SSTs (Biasutti and Giannini 2006). The 1980s Sahel drought—the most intense episode of the twentieth century—has been attributed to the circulation change associated with Indian Ocean warming (Hagos and Cook 2008), and the drought recovery linked to higher levels of greenhouse gases in the atmosphere (Dong and Sutton 2015). Sahel rainfall has also been linked to Atlantic multidecadal oscillation (AMO) variability (Knight et al. 2006; Zhang and Delworth 2006; Mohino et al. 2011; Nigam et al. 2011; Martin and Thorncroft 2014; Nigam and Ruiz-Barradas 2016), with the cold AMO phase coincident with extended droughts over the Sahel.

Causes of surface temperature variability are less well established (Collins 2011), although an amplified warming signal has been detected over the Sahara Desert in recent decades (Cook and Vizy 2015; Zhou 2016; Vizy and Cook 2017).

The importance of agriculture in the African economies warrants a seasonally resolved analysis of hydroclimate variability and change over the African continent. The seasonality of trends in temperature and precipitation over Africa has been briefly examined in earlier studies. Temperature trends over the continent as a whole were found to be greater in summer and fall than in winter and spring (Collins 2011; Hulme et al. 2001), with significant winter warming in northern tropical Africa and significant summer warming across the continent, and specifically the Sahara (Collins 2011). Documented precipitation trends, other than over the Sahel, include the decreasing spring rainfall trend over East Africa (Williams and Funk 2011; Rowell et al. 2015; Maidment et al. 2015) and continental-scale seasonal precipitation trends (Hoerling et al. 2006); the latter have been plotted but not extensively discussed. The need for analyzing seasonal rainfall in tropical regions has been noted (Feng et al. 2013).

Global climate change often leads to the wet regions getting wetter and the dry ones drier (Chou et al. 2013), suggesting adverse impacts on deserts. The impact on the Sahara is of great importance for the proximal countries in northern Africa as well as for remote regions through the influence of Saharan dust on SSTs and Atlantic hurricane activity (Evan et al. 2016). Previous studies have estimated the size of the annual-mean Sahara Desert (Tucker and Nicholson 1999; Tucker et al. 1991) but only over the recent satellite-era periods ranging from 10 to 17 years. The century-long seasonal trends in the expanse and extent of the Sahara Desert, whose structure and mechanisms concern this study, have hitherto remained undocumented to the best of our knowledge. A seasonally stratified perspective is at some variance with the classical notion of the desert (based on an annual-mean view) but is nonetheless pursued in the interest of agriculture and water resource planning. It is, of course, complemented by analyses of the annual-mean hydroclimate trends, yielding twentieth-century expansion rates for the conventionally defined Sahara Desert.

The present study expands on previous work by examining the regional structure of the century-long seasonal trends in temperature and precipitation over the African continent, with the Saharan expanse being one of the foci. Characterization of the trends is a necessary first step before investigation of the underlying mechanisms; a follow-on study targeting the mechanisms is planned. The datasets and analysis methods are described in section 2. The seasonal climatology of near-surface air temperature (SAT) and precipitation over the African continent are outlined in section 3 to provide context for characterization of the century-long seasonal hydroclimate trends in section 4. Expansion of the Sahara Desert over the twentieth century is discussed in section 5, and the winter and summer expansion mechanisms are investigated in section 6. An assessment of the seasonal temperature and precipitation trends over the African continent in the twentieth-century historical simulations from five climate models used in the IPCC Fifth Assessment Report (AR5) are shown in section 7. Concluding remarks, including the influence of multidecadal SST variability on the Sahara Desert's twentieth-century expansion rate, and plans for future work follow in section 8.

2. Datasets and analysis method

The study focuses on centennial trends rather than multidecadal variability (a more common analysis focus) of African hydroclimate. Linear trends in temperature and precipitation are computed from least squares fitting using seasonally averaged data. To avoid confusion given Africa's expansive footprints in both hemispheres,

seasons are referred using their boreal definition: Winter is the average of December, January, and February (DJF), and so on. For the historical climate simulations, linear trends are computed by averaging the linear trends manifest in the ensemble members of that model.

a. Observational datasets

Three independent analyses of the observed SAT are used in this study: The CRU TS4.00 monthly analysis from the Climate Research Unit of the University of East Anglia (Harris et al. 2014) is available on a 0.5° continental grid for the January 1901–December 2014 period, from http://www.crudata.uea.ac.uk/cru/data/hrg/cru_ts_4.00/. Berkeley Earth's monthly analysis of surface temperature anomalies relative to the 1951–80 climatology (Rohde et al. 2013) is available on a 1.0° grid for the period January 1850–December 2015; it is downloadable from http://berkeleyearth.org/data/. Finally, the NASA Goddard Institute for Space Studies (GISS) analysis of SAT anomalies relative to the 1951–80 baseline (Hansen et al. 2010) is available on a 2.0° land–ocean grid for the January 1880–September 2015 period from http://www.esrl.noaa.gov/psd/data/gridded/data.gistemp.html. The datasets are converted to a common 0.5° resolution using bilinear spatial interpolation. The number of missing data points in space and time, or data density, is assessed for each SAT analysis and reported in the appendix A.

The Global Precipitation Climatology Centre (GPCC; Becker et al. 2013) provides a monthly analysis of precipitation from quality-controlled rain gauge data; GPCC's Full Data Reanalysis version 7 data are available on a 0.5° continental grid from January 1901 to December 2013, from http://www.esrl.noaa.gov/psd/data/gridded/data.gpcc.html#detail. The monthly precipitation database informing the GPCC analysis is, perhaps, the largest among competing analyses (Schneider et al. 2014, their Fig. 2), prompting its use in constraining NASA's Tropical Rainfall Measuring Mission (TRMM) precipitation (https://mirador.gsfc.nasa.gov/collections/TRMM_3B42_daily__007.shtml). Sahel rainfall is defined as the area-averaged rainfall within 20°W–40°E and 10°–20°N, following Held et al. (2005).

The NCEP–NCAR reanalysis (Kalnay et al. 1996) is used for calculating the core latitude of the subtropical tropospheric jet in northern winter, following the method of Archer and Caldeira (2008) with integration over the latitude band 15°–45°N. The 2.5° resolution reanalysis is obtained from http://iridl.ldeo.columbia.edu/SOURCES/.NOAA/.NCEP-NCAR/.CDAS-1/.MONTHLY/.

Several climate indices are used in the study: The Atlantic multidecadal oscillation (Enfield et al. 2001; Kavvada et al. 2013) index was computed as the linearly detrended seasonal SST anomaly over the North Atlantic (0°–60°N, 75°–5°W), following Enfield et al. (2001); SST from the HadISSTv1.1 analysis (Rayner et al. 2003) was used. An additional marker of AMO variability was the principal component extracted from an extended empirical orthogonal function (Weare and Nasstrom 1982) analysis of HadISSTv1.1 SST data (Guan and Nigam 2009; A. Sengupta et al. 2018, unpublished manuscript). The Pacific decadal oscillation (PDO) index was obtained from http://jisao.washington.edu/data/pdo/ where it is defined as the leading principal component of monthly SST anomalies in the North Pacific basin (poleward of 20°N; Zhang et al. 1997).

Streamflow data for the Niger River were obtained from NCAR's monthly flow rate archive (https://rda.ucar.edu/datasets/ds552.1/; Dai and Trenberth 2003). Station 9142 (Koulikoro; 12.887°N, 7.54°W) was used as it has the longest record among stations in the source region of the Niger River. The record extends from January 1907 to December 1990.

b. Historical climate simulations

Simulations of twentieth-century climate forced by historical greenhouse gas emissions, aerosol loadings, and solar activity are referred to as historical climate simulations (Taylor et al. 2012). In this study, five models contributing to the IPCC AR5 are analyzed: NCAR's CCSM4, which is available for the 1850–2005 period on an approximate 1.25° × 0.942° longitude–latitude grid; NOAA's GFDL CM3, which is available for the 1860–2004 period on a 2.5° × 2.0° grid; the Met Office's HadCM3, which is available for the 1860–2005 period on a 3.75° × 2.5° grid; the Met Office's HadGEM2-ES, also available for the same period but on 1.875° × 1.25° grid; and the Max Planck Institute's MPI-ESM-LR simulation, which is available for the 1850–2005 period on an approximate 1.875° × 1.865° grid. (Expansions of acronyms are available online at http://www.ametsoc.org/PubsAcronymList.)

c. Desert expansion

Two methods are used to quantify desert expansion during the 1902–2013 period. In both methods, a precipitation threshold is chosen to define the desert boundary; two threshold values—100 mm yr^{-1} (or 0.274 mm day^{-1}) and 150 mm yr^{-1} (or 0.411 mm day^{-1})—based on previous definitions of the annual-mean Sahara boundary (e.g., Tucker and Nicholson 1999; Breman and deWit 1983) are used. Two thresholds were considered so that sensitivity of the desert-area trend to the desert definition can be assessed. Desert area is computed by taking an area sum after weighting each grid-cell area

by the cosine of its latitude; the Grid Analysis and Display System (GrADS) function asum was used. In the first method, referred to as the area-trend method, the desert area is computed each year in each of the four seasons and annually, with average rainfall less than 0.274 mm day^{-1} (0.411 mm day^{-1}) defining deserts. The 1902–2013 linear trend in the computed area characterizes desert expansion/contraction over the twentieth century.

In the second method, referred to as the endpoint method, the precipitation climatology (P_{clim}) and the linear trend in precipitation (P_{trend}) over the 112-yr record are first computed at each grid point, seasonally and annually. These are used to create two maps, showing precipitation at the end (from the plus sign in the following expression) and at the beginning (from the minus sign) of the record, $P = P_{\text{clim}} \pm (P_{\text{trend}}) \times 56$ yr. The desert extent is then mapped in these synthetic 1902 and 2013 precipitation distributions at the endpoints of the record based on the chosen threshold, with the difference yielding desert expansion over the time period.

In both methods, the desert area computation is restricted to North Africa (northward of 5°N) to preclude inclusion of the Namib–Kalahari Desert, and to the west of 43°E to avoid inclusion of the Horn of Africa.

Each method has its advantages: The area-trend method is conceptually simple, but it does not reveal the desert advance and retreat regions. The endpoint method is slightly more complex but it easily outlines the desert advance/retreat regions. Both methods should yield similar results except, perhaps, when the analysis period is comparable to the embedded variability time scales—a condition met with the AMO, especially when it is influential on regional hydroclimate. The aliasing of multidecadal variability into linear trends would be inevitable in this case but with the two methods having different exposure to aliasing from the inverted order of the area-computation and linear-trend operations.

The seasonal northern edge of the Sahara Desert was computed each year as follows: For each desert longitude (20°W–35°E), the nearest latitude north of 20°N where the seasonal precipitation threshold was met was determined. The latitudes were then averaged to obtain the northern edge of the Sahara Desert.

d. Statistical significance

Statistical significance of individual linear trends at the 95% confidence level was assessed using the so-called AdjSE+AdjDF approach of Santer et al. (2000). This method employs an effective sample size based on the lag-1 autocorrelation coefficient of the regression residuals. The statistical significance of correlation coefficients was calculated using the method outlined in Ebisuzaki (1997), which is useful for time series with high serial correlation. Significance of the correlation coefficients is noted in the text.

3. Seasonal climatology

The seasonal cycle of rainfall over the African continent is shown in Fig. 1. Rainfall is larger, not surprisingly, in the summer hemisphere: over tropical West Africa, the Sahel, and Ethiopia in boreal summer (JJA) and over the Congo and Zambezi basins in austral summer (DJF). The similarity of the March–May and September–November rainfall distributions—with equatorial Africa, especially the Congo basin, being the rainfall focus—reflects the similar insolation distribution over the continent at these times from the Sun being overhead twice at the equator each year, during the vernal (late March) and autumnal (late September) equinox. The Sahara Desert is, however, drier in spring than it is in fall, and the Namib–Kalahari Desert likewise is drier in its spring than fall. The strong latitudinal gradient in precipitation at the southern boundary of the Sahara is a notable feature in all seasons, with the movement of this gradient over time having implications for regional agricultural productivity.

The desert boundary, based on seasonally averaged rainfall threshold of 0.274 mm day^{-1} (or 25 mm season^{-1}), is shown in thick black contours in Fig. 1; boundaries based on the annual-mean threshold of 0.274 mm day^{-1} are shown in Fig. C1 in appendix C. The Sahara expanse is largest in boreal winter and smallest in boreal fall (see Table 1); the larger threshold (0.411 mm day^{-1} or 37.5 mm season^{-1}) yields the smallest expanse in summer; both analysis methods return the same seasons for maximum and minimum expanse (cf. Table 1). In winter, the dry region extends from ~10° to ~30°N, but in summer the Sahel rainfall pushes the Sahara's southern edge closer to 20°N. Likewise, the Namib–Kalahari Desert in Southern Hemisphere Africa is most expansive in austral winter, consistent with the notion of the desert location under the descending branch of the meridionally overturning Hadley circulation; the Hadley descent is most intense in each hemisphere's winter (e.g., Nigam and Chan 2009).

The seasonal distribution of climatological SAT is also shown in Fig. 1, using red contours. The warmest temperatures are found in boreal summer when SAT exceeds 33°C over western Saharan Africa. The coldest temperatures occur northward of the Atlas Mountains in Algeria and Morocco in boreal winter. A local

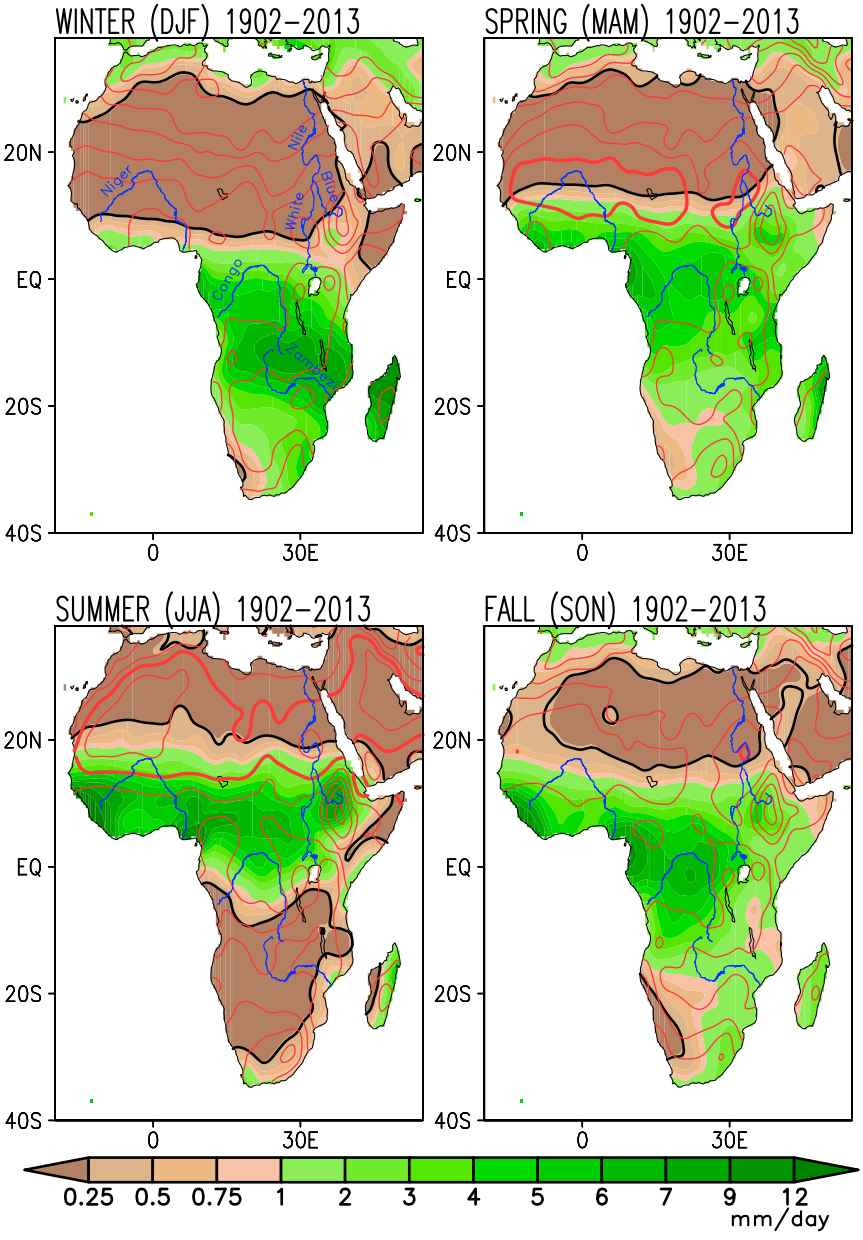

FIG. 1. Seasonally averaged precipitation (brown–green shading; mm day^{-1}) and surface air temperature (SAT; red contours; °C) for the period 1902–2013. Precipitation is from GPCC and SAT from the CRU TS4.00 dataset. The nonuniform shading interval for precipitation is indicated through the color bar. Contour interval for SAT is 3.0°C. Fields are shown after nine applications of the 9-point smoother (smth9) in GrADS. Thick red contours indicate the 30°C isotherm, while thick black ones mark the 0.274 mm day^{-1} precipitation isoline. Note that 0.274 mm day^{-1} is equivalent to 100 mm yr^{-1}, a precipitation-based definition of the annual-mean Sahara Desert boundary (Tucker and Nicholson 1999). Major rivers are shown in thin blue lines and with names labeled in the top-left panel.

minimum in SAT exists over Ethiopia in all four seasons due to the high elevation of the Ethiopian Highlands. The spring and fall distributions exhibit less similarity in SAT than in rainfall, especially over sub-Saharan Africa where SAT is notably higher in boreal spring, likely because of the preceding dry season (winter) and depleted soil moisture stores, which would preclude latent disposition of increased spring insolation.

4. Centennial trends in surface air temperature and precipitation

The 1902–2014 period linear trend, obtained by averaging the linear trend in three independent analyses of SAT observations, is shown in Fig. 2. Notable features include the following:

- Larger trends over Northern Hemisphere Africa, in all seasons.
- A regional maximum over Sudan, particularly, in spring when SAT trends are larger than 1.5°C century^{-1}; interestingly, this is the Nile River basin.
- A pronounced seasonality in trends over North Africa, near Algeria and Tunisia. Trends here range from ~0.8°C century^{-1} in winter to as much as 2.0°C century^{-1} in summer.
- A comparatively muted seasonality in trends over Southern Hemisphere Africa except for Angola, Namibia, and Botswana where austral winter (JJA) warming is stronger than in other seasons.
- The similarity in boreal winter and fall SAT trends over much of the continent.

The seasonality of SAT trends can potentially modulate the amplitude of the seasonal cycle of SAT in the recent period. An increasing amplitude can worsen heat stress, as over central-southern Sudan (to the west of the White Nile) where twentieth-century SAT trends are large, especially in spring when the SAT peaks climatologically as well (cf. Fig. 1), leading to hotter springs and increased heat stress. Likewise, over northern Africa, including Algeria, Tunisia, and Libya, SAT trends are largest in summer, the season of greatest climatological SAT. In both these regions, the SAT trends amplify the seasonal cycle of regional SAT, intensifying heat extremes. (Modest differences in the twentieth-century SAT trends in three independent analyses of SAT observations are shown in Fig. A1 of appendix A, for reference.)

The linear trend in seasonal precipitation over the twentieth century (1902–2013) is shown in Fig. 3 against the backdrop of the climatological dry regions (brown hatching). The centennial trends show interesting variations, corroborating the importance of seasonal analysis. For example, over Kenya and Tanzania, declining rainfall trends are present in boreal spring whereas increasing ones are present in fall and winter, each with socioeconomic implications. An annual-mean perspective, where offsetting seasonal trends average out, is not sufficient to understand the impact of climate change on a continent where the seasonal rhythm of rainfall is the pace maker.

The rainfall decline is notably intense, with no seasonal offsets, over tropical West Africa. The decline is broadly focused on the source region of the Niger River, extending across several Gulf of Guinea rim countries (Senegal, Gambia, Guinea-Bissau, Guinea, Sierra Leone, Liberia, and Cote d'Ivoire). The rainfall decline exceeds 1.0 mm day^{-1} century^{-1} here (i.e., a 10%–25% decline in seasonal rainfall over the course of the twentieth century). The boreal spring decline is most impressive, percent-wise, and must lead to an increasing delay in the build-up of Niger streamflow after the dry winter season (see Fig. B1).

Another region showing rainfall decline in all seasons is the Congo River basin, especially the part encompassing Angola and the Democratic Republic of the Congo. Rainfall decline here is impressive in the shoulder seasons (spring and fall), with trends exceeding 0.6 mm day^{-1} century^{-1} where seasonal rainfall is ~6.0 mm day^{-1}. The thick brown lines in Fig. 3 mark the climatological dry zones, facilitating a visual assessment of desert expansion–contraction over the twentieth century (the focus of the next section).

The African Great Lakes region, especially Victoria and Tanganyika, is one of the few regions on the continent exhibiting increasing twentieth-century rainfall, mostly in austral spring and summer. This is interesting because of the proximity of this region to the source of the Nile River, and implications for streamflow in the downriver region.

The advantages of a seasonal rather than an annual-mean perspective in the context of centennial change in regional hydroclimate over Africa can be gleaned from a comparison of Figs. 2 and 3 with their annual-mean counterparts (see Fig. C1).

5. Change in Sahara Desert expanse over the twentieth century

The overlay of twentieth-century precipitation trends on the climatological dry zones in Fig. 3 suggests that the Sahara Desert has expanded both equatorward and northward. The Sahara's extent has been investigated using vegetation-zone boundaries as markers of desert expanse and its interannual variation (Tucker and Nicholson 1999; Tucker et al. 1991). Although interesting because of the implicit seasonal context, these studies analyzed short records such as the recent 10–17-yr-long satellite-era ones. Unfortunately, desert trends over such periods reveal little about the secular changes in the Sahara because of the potential aliasing of decadal to multidecadal variability into short-period trends.

Here, we use the precipitation rate to demarcate the desert region. The use of precipitation rather

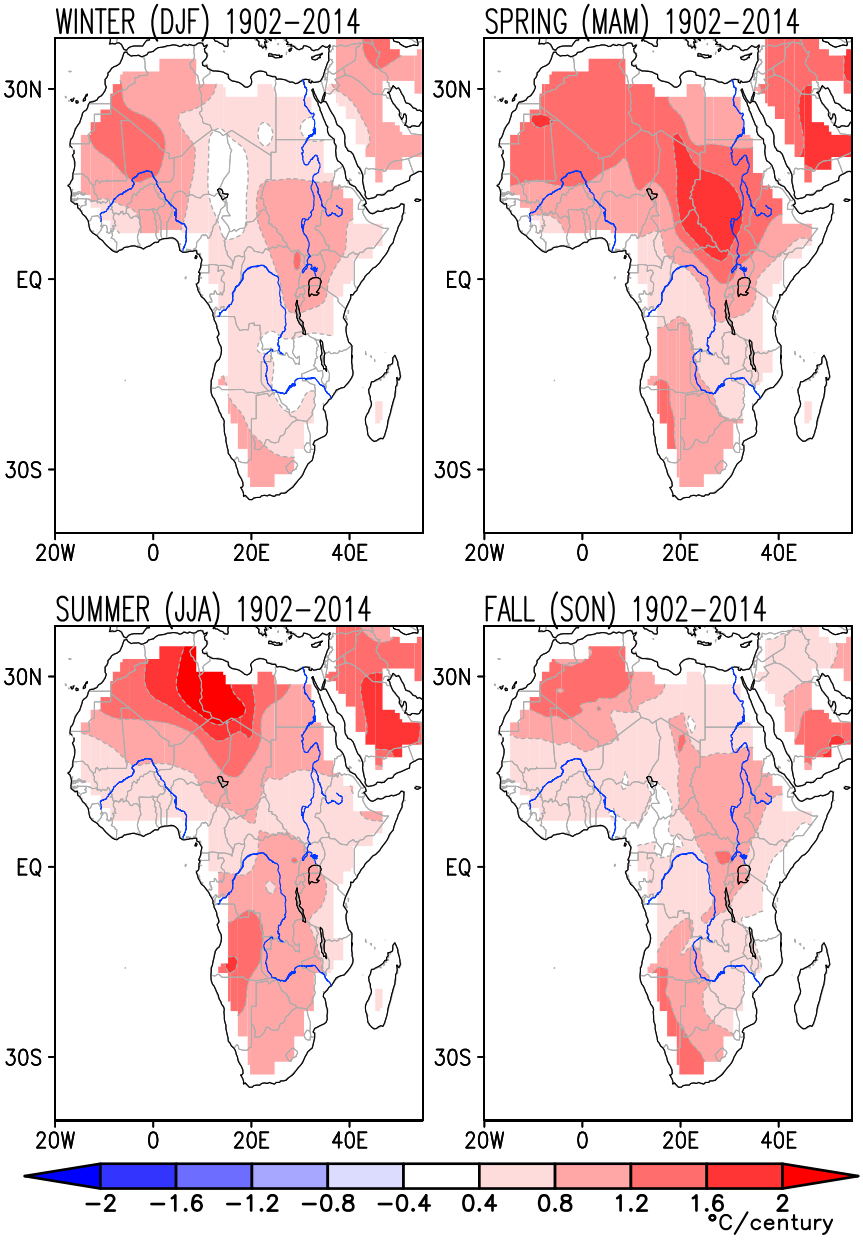

FIG. 2. Linear trends in near-surface air temperature over the African continent during 1902–2014. Average of the trends in three independent SAT analyses—CRU TS4.00, Berkeley Earth, and NASA GISS—is shown after each was interpolated to 0.5° resolution. Contour and shading are at 0.4°C century^{-1} interval. Fields are shown after nine applications of the 9-point smoother (smth9) in GrADS. Country boundaries are shown in thin gray and major rivers in thin blue lines.

than vegetation allows analysis of a longer record notwithstanding the spatiotemporal sparseness of the precipitation record in the early twentieth century. A direct relationship between precipitation and the vegetation index found in previous studies (Tucker and Nicholson 1999; Tucker et al. 1991) supports such a strategy. In Fig. 3, a 100 mm yr^{-1} (or 0.274 mm day^{-1}; one of the two thresholds discussed in section 2c) precipitation isoline demarcates the deserts, seasonally (and in Fig. C1, annually). A light brown hatching of the regions where climatological precipitation is less than this value marks the desert expanse, which is monitored using the two methods discussed in section 2.

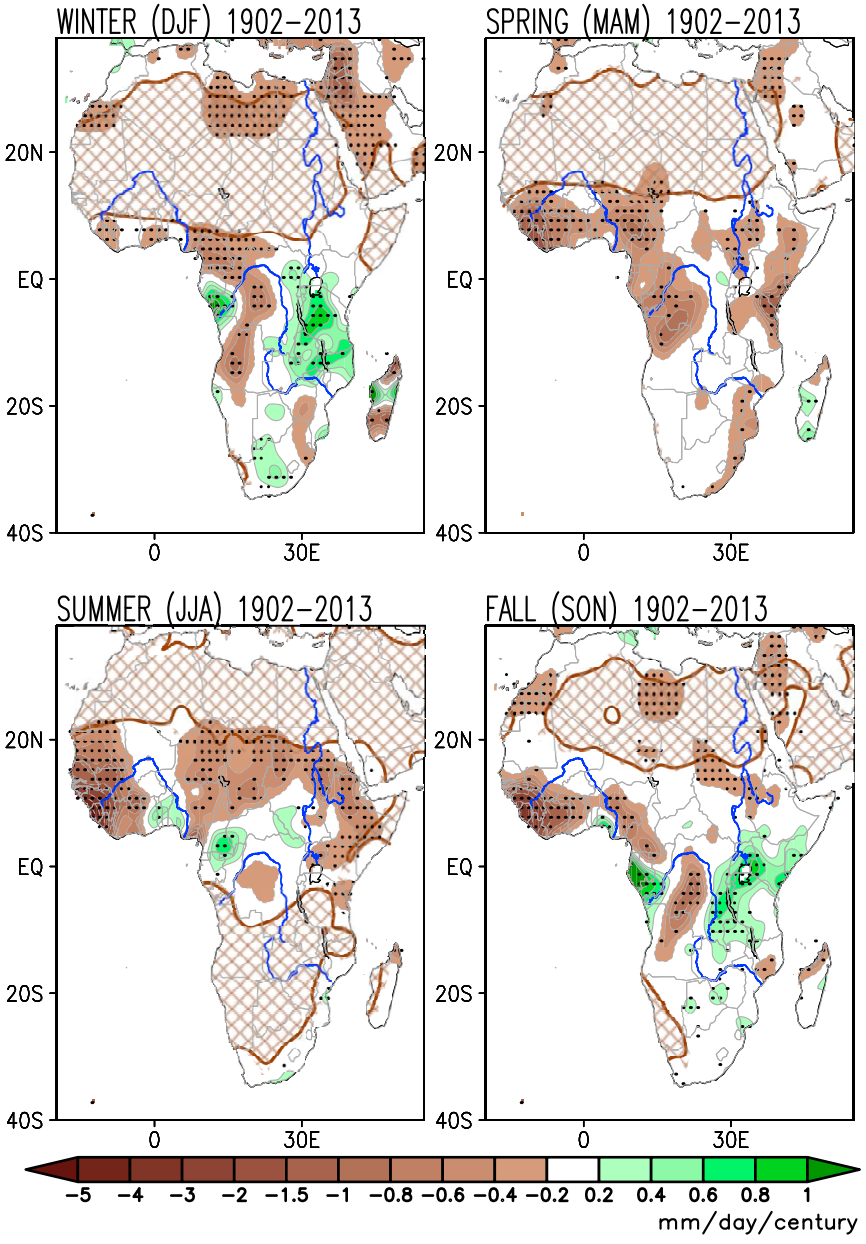

FIG. 3. Linear trends in seasonal precipitation over the African continent during 1902–2013, from the 0.5° resolution GPCC dataset (mm day^{-1} century^{-1}). The nonuniform contouring and shading interval is indicated via the color bar. Thick solid brown contours mark the 0.274 mm day^{-1} climatological precipitation isoline, and brown hatching indicates regions where climatological precipitation is below 0.274 mm day^{-1} (or 100 mm yr^{-1})—a precipitation threshold used for defining the Sahara Desert. Fields are shown after nine applications of the 9-point smoother (smth9) in GrADS. Trends significant at the 95% confidence level are denoted with black dots. Major rivers are shown in thin blue lines and country boundaries in thin gray lines.

a. The Sahara's advance

The twentieth-century change in the Sahara Desert's seasonal and annual extent is displayed in Figs. 4 and 5; the change is estimated using the endpoint method. Brown shading, which represents the desert's advance over the century, shows significant northward creep in boreal winter albeit not uniformly across longitudes; hefty footprints over Libya and Algeria in the central sector, and over the western Sahara and Mauritania to the west, characterize the northward expansion in winter. The desert has encroached equatorward as well

in winter, with notable intrusions in Nigeria, Cameroon, and the Central African Republic.

The centennial change in the Sahara's summer extent is through the equatorward advance of its southern boundary (Fig. 4) which is climatologically located at ~20°N because of robust summer rainfall in the northern tropics including the Sahel (0°–20°N; cf. Fig. 1). Much as with the winter desert advance at the northern boundary, the southern advance is sectorally focused, with intrusions in Mauritania to the west and Niger and Chad in the central sector. The countries most impacted by the Sahara Desert's seasonal and annual-mean advance are listed in Table 1.

Note that a similar demarcation of the Sahara Desert advance is obtained from the independently analyzed University of Delaware precipitation dataset (Willmott and Matsuura 2015; not shown), allaying dataset dependency concerns.

The annual-mean desert advance (using the 100 mm yr^{-1} threshold; see Fig. 5), provides context for the seasonal analysis and comports with the canonical desert definitions based on the annual-mean rainfall threshold (e.g., Tucker and Nicholson 1999). The annual-mean advance shows primarily southward creep relative to the annual-mean desert boundaries (see Fig. C1).

b. *The Sahara's expanse*

A quantitative analysis of the centennial change in the Sahara Desert's seasonal and annual-mean expanse is reported in Table 1. The primary analysis is based on the area-trend method but the endpoint method that generated Figs. 4 and 5 is also used with both desert definitions to assess the sensitivity of the desert expansion to analysis methods; the sensitivity to analysis period is discussed in section 8. As noted above, the expansion has been largest (area-wise) in boreal winter (2 246 000 km^2, a 16% increase) and smallest in summer (876 000 km^2, an 11% increase) using the area-trend method with a 100 mm yr^{-1} threshold. Estimates of desert expansion from the endpoint method (noted in parentheses in Table 1), with the same threshold, yield maximum desert expansion in winter (2 348 000 km^2, an 18% increase) and a minimum in spring (1 132 000 km^2, an 11% increase). The endpoint method, however, yields significantly larger expansions in boreal summer and fall. As noted in section 2, the two estimates can differ when multidecadal variability is potentially aliased into centennial trends—the case in summer and fall when the 65–70-yr time scale AMO variability (e.g., Schlesinger and Ramankuttty 1994; Kavvada et al. 2013) exerts strong influence on Sahel rainfall (e.g., Zhang and Delworth 2006; Nigam and Ruiz-Barradas 2016). Percent-wise, the desert expansion is largest in boreal fall from both methods.

The sensitivity of the desert expansion rate to the desert-defining precipitation-threshold is also reported in Table 1. A less stringent definition, based on a 150 mm yr^{-1} threshold, leads to more expansive deserts, not surprisingly, but also to smaller centennial expansions, indicating a tightening of the meridional precipitation gradient over the century. Percentages drop on both counts but the Sahara's expansion remains robust with the largest expansion, as before, in boreal winter (1 800 000 km^2, a 12% increase); this winter expansion, from the area-trend method, is largest both area- and percent-wise. The weakest expansion again is in summer (847 000 km^2, a 10% increase). Results from the endpoint method using the larger threshold are qualitatively similar to those obtained with the lower one.

The sensitivity analysis indicates that while desert expansion and the related area percentage vary somewhat with the desert definition and analysis method, one can reasonably conclude that the Sahara Desert has grown larger, area-wise, more in winter than in summer; percentage-wise, the summer expansion can be larger in view of the smaller (nearly halved) climatological desert expanse in summer. The countries bearing the brunt of the Sahara's northwestward–northward advance in fall–winter are Libya, Mauritania, and Western Sahara; the southern advance principally impacts Niger, Chad, and Mauritania in summer, and Sudan in fall. One would be remiss to not note the summer desertification in the Horn of Africa, especially Ethiopia and Somalia. Notable against this backdrop of widespread desert advance (brown shading) over the northern continent is a sliver of green over Mali in fall, reflecting the Sahara's retreat.

The expansion of the Sahara Desert is also analyzed using the conventional annual-rainfall based desert definition. Table 1 (last column) notes the findings from the area-trend and endpoint methods for both the 100 and 150 mm yr^{-1} annual-rainfall thresholds. A slightly shorter period, beginning in 1920, is analyzed in the annual case in order to focus on the relatively stable rain gauge network period (S. Nicholson 2018, personal communication). During 1920–2013, the Sahara expanded by over 700 000 km^2 (or ~7600 km^2 yr^{-1}) based on the 100 mm yr^{-1} definition, indicating a ~10% expansion over its climatological area (7 426 000 km^2). The desert's southward creep (cf. Fig. 5) is the major contributor (~554 000 km^2 or 7.5%) to the expansion; the northward advance (182 000 km^2) contributes the remaining 2.5%. The linear trend in the Sahara Desert's expanse is sensitive to the analysis period

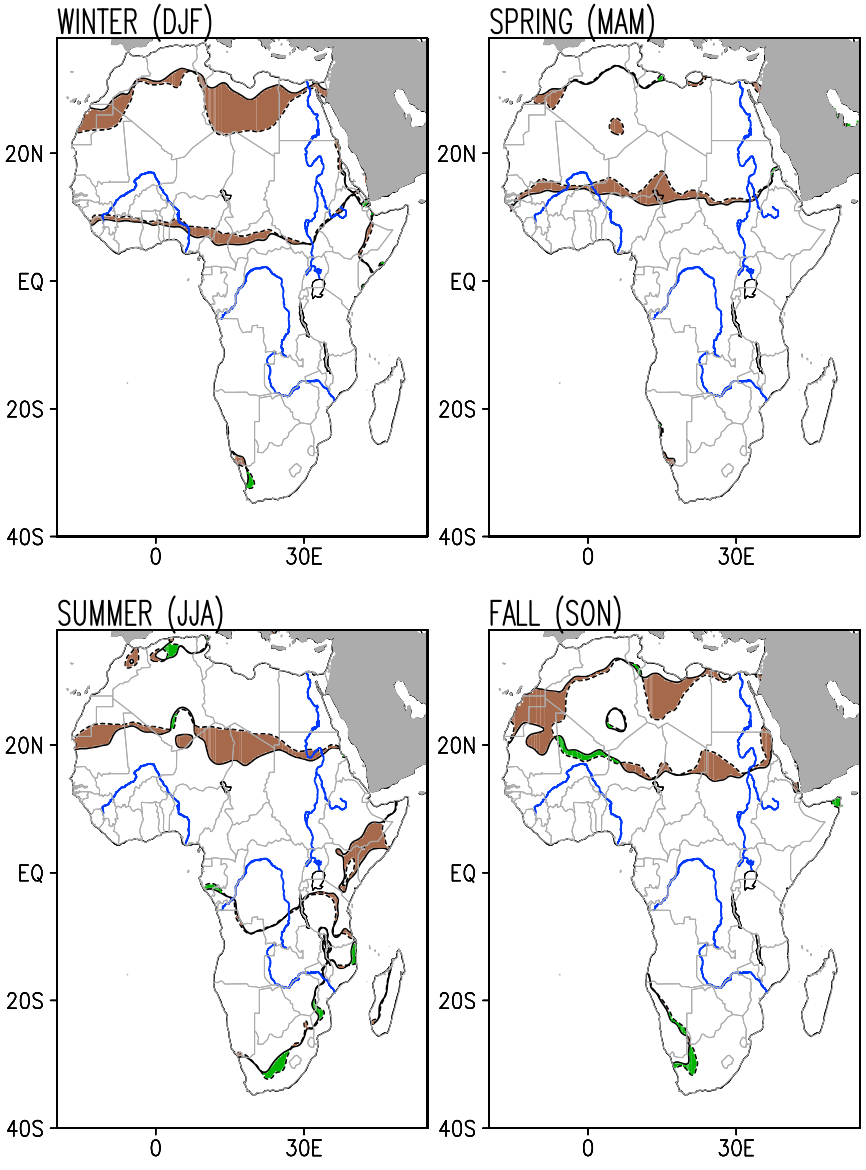

FIG. 4. Advance or retreat of the Sahara Desert over the 1902–2013 period, seasonally. The dashed (solid) brown lines denote the 0.274 mm day^{-1} precipitation isolines in the synthetic 1902 (2013) precipitation map obtained from the endpoint analysis (cf. section 2). The brown (green) shaded areas denote desert advance (retreat). (Note that the observed precipitation distribution at the period endpoints cannot be directly used as it includes both interannual and decadal–multidecadal variability components.)

from the potential aliasing of multidecadal variability, as noted earlier and as further discussed in section 8 (and Fig. 8).

Unlike northern Africa, the southern continent is devoid of any desert advance, in any direction or season. To the contrary, the Namib/Kalahari Desert is found retreating, albeit modestly, in austral winter (JJA) and spring (SON) when it is, climatologically, most expansive (cf. Fig. 1).

6. The Sahara's expanse: Variation and potential mechanisms

The Sahara Desert's expanse during the 1902–2013 period, and not just at its endpoints, is the focus of this section. The desert expanse in winter and summer is plotted in Fig. 6, along with select indices of circulation and SST variability that can provide insights on causal mechanisms.

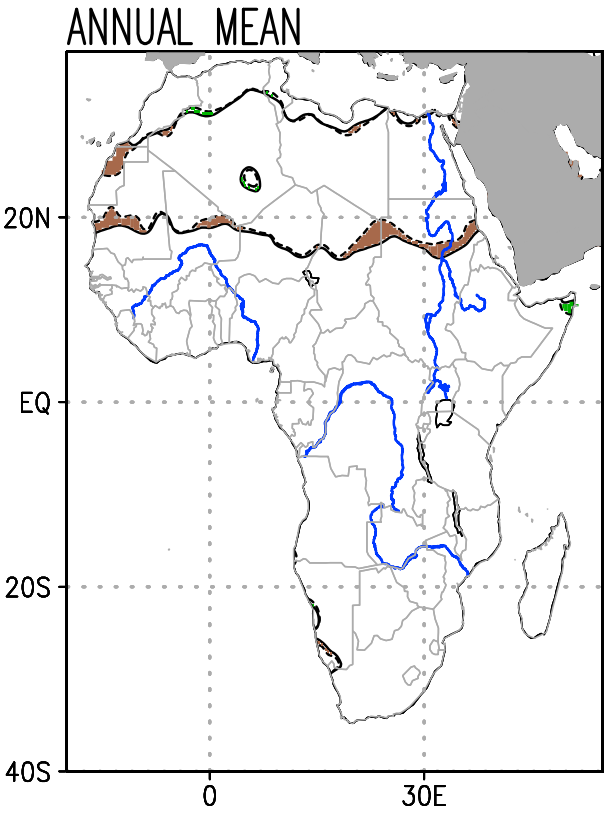

FIG. 5. As in Fig. 4, but for the advance or retreat of the Sahara Desert over the 1920–2013 period, annually. Desert identification here is fully consistent with the canonical desert definition based on annual-mean rainfall: a 100 mm yr^{-1} threshold is used.

a. Winter variation

The Sahara's winter expanse (Fig. 6, top) is plotted together with the average latitude of the desert's northern edge using methods described in section 2. The location of the northern edge is of interest because the endpoint analysis (Fig. 4) showed the twentieth-century expansion to be, principally, through the northern boundary. Not surprisingly, winter variations in the Sahara Desert expanse correlate well with the latitudinal position of the desert's northern boundary (Fig. 6, top); $r = 0.94$ (0.88) for smoothed (unsmoothed) indices; note that the high, statistically significant correlation emerges not just from similar upward trends but also from the correspondence in decadal variations. The linear fit to the Sahara's winter expanse is shown by the thin black line, which is the basis for the area-trend analysis (Table 1).

We hypothesize that the Sahara Desert's northward expansion in winter is due, largely, to the widening of the tropics (Seidel et al. 2008), based on canonical understanding of the desert's location (cf. section 3) relative to the descending branch of the Hadley circulation. As the descending branch terminus, which defines the width of the tropics, dynamically, is collocated with the core latitude of the subtropical jet in the upper troposphere (e.g., James 2003), the latter serves as a convenient proxy for the width of the tropics. Previous studies have shown that the core of the northern winter subtropical jet has moved poleward in recent decades (Archer and Caldeira 2008). The 30°W–60°E sector-averaged latitudinal position of the jet in the NCEP–NCAR reanalysis (Kalnay et al. 1996), computed using these authors' method, is shown by the red line in Fig. 6 (top), along with a linear fit to its variation. While both the Sahara's expanse and the subtropical jet-latitude depict upward trends—and nearly identical ones (0.98% and 1.05% yr^{-1}, respectively) when for the same period (1949–2013)—the two variations are modestly correlated ($r = 0.25$; not significant at the 95% level), notwithstanding periods (1950–65 and 1985–2013) when they track each other closely. The similar upward trends over the recent 65-yr period lend credence to the hypothesis linking the Sahara's increasing winter expanse (and northern extent) to a secular change in the width of the tropics. The modest correlation between the two on decadal (and shorter) time scales, while detracting, attests to the influence of other processes on the desert expanse in winter, such as tropical SSTs and the North Atlantic Oscillation (through its impact on winter storm tracks; e.g., Linkin and Nigam 2008).

b. Summer variations

Summer variations in the Sahara Desert's expanse, unlike winter ones, arise mainly from the north–south movements of its southern boundary which borders the Sahel. The summer expanse (solid black line) exhibits both an upward trend, highlighted by the linear fit (thin black straight line), and notable decadal–multidecadal variations. As areal changes result from the equatorward advance or poleward retreat of the desert's southern edge, the Sahara's summer expanse should be inversely linked to Sahel rainfall (defined in section 2a), which is plotted with a dashed black line. The inverse relationship can be visually discerned: for example, the drying of the Sahel (a multidecadal decline in Sahel rainfall from the mid-1950s to the mid-1980s) is coincident with the Sahara's expansion; the full-period correlation ($r = -0.80$; significant at the 95% level) points to a strong inverse relationship. The anticorrelation allows tapping into extensive analyses of Sahel rainfall variability in the attribution of the summer waxing and waning of the Sahara Desert.

The Sahel rainfall has been linked to AMO variability among other processes, as noted in the introduction. To

TABLE 1. Expansion of the Sahara Desert: seasonally during 1902–2013 and annually during 1920–2013, based on the movement of the 100 and 150 mm yr^{-1} precipitation isolines. The expansion is computed using both area-trend and endpoint methods; endpoint values are in parentheses. Both methods are described in section 2. The areal values are rounded off to the nearest 1000 km^2 (which is about 1/3 of the 0.5° grid cell area at the equator). DJF refers to boreal winter months (December, January, and February), and so on. The impacted countries are identifiable only from the endpoint method; the ones in boldface are the most impacted by desert advance.

	Threshold (mm yr^{-1})	Winter (DJF)	Spring (MAM)	Summer (JJA)	Fall (SON)	Annual (1920–2013)
Climatological Sahara extent (km^2)	100	13 686 000 (12 868 000)	10 540 000 (9 979 000)	7 725 000 (6 198 000)	7 583 000 (6 136 000)	7 426 000 (6 890 000)
	150	14 557 000 (13 872 000)	11 420 000 (10 782 000)	8 492 000 (7 351 000)	8 736 000 (8 018 000)	8 528 000 (7 947 000)
Sahara expansion (km^2)	100	2 246 000 (2 348 000)	1 287 000 (1 132 000)	876 000 (1 594 000)	1 354 000 (2 048 000)	711 000 (738 000)
	150	1 800 000 (1 433 000)	1 009 000 (627 000)	847 000 (1 478 000)	999 000 (1 366 000)	718 000 (549 000)
Sahara expansion (% of climatological area)	100	16% (18%)	12% (11%)	11% (26%)	18% (33%)	10% (11%)
	150	12% (10%)	9% (6%)	10% (20%)	11% (17%)	8% (7%)
Countries affected		**Libya,** Egypt, Tunisia, Algeria, Morocco, **Western Sahara,** Mauritania, **Central African Rep.**, **Cameroon**, Nigeria, Guinea, Cote D'Ivoire, Ghana, Togo, and Benin	Morocco, Sudan, **Chad, Niger**, Nigeria, Burkina Faso, **Mali**, Senegal, and Guinea	**Mauritania**, Western Sahara, Mali, Algeria, **Niger**, **Chad**, Libya, and Sudan	**Libya**, Egypt, Algeria, Morocco, **Western Sahara**, **Mauritania**, Niger, Chad, and **Sudan**	Libya, Egypt, Algeria, **Western Sahara**, **Mauritania**, **Mali**, Niger, **Chad**, and **Sudan**

assess links between AMO and the Sahara's extent, two markers of AMO variability are plotted in Fig. 6 (bottom) along with their correlations to the Sahara's expanse and Sahel rainfall. The AMO SST principal component (dashed red line), obtained from an evolution-centric spatiotemporal analysis of seasonal SST anomalies in the twentieth century (Guan and Nigam 2009; A. Sengupta et al. 2018, unpublished manuscript), shows higher correlations with both the Sahara's expanse ($r = -0.37$; significant at the 80% level) and Sahel rainfall ($r = 0.53$; significant at the 95% level) in boreal summer.

Decadal SST variability in the Pacific basin, as typified by the Pacific decadal oscillation (Mantua et al. 1997), is also linked with Sahel rainfall (Villamayor and Mohino 2015; Nigam and Ruiz-Barradas 2016) albeit not as strongly as the AMO. The PDO index, shown in Fig. 6 (solid blue line), is correlated with Sahel rainfall and the Sahara's expanse at −0.33 (significant at the 90% level) and 0.27 (significant at the 75% level), respectively. A statistical link between the PDO and Sahel rainfall seems more intriguing than the rainfall's link with the AMO because the AMO SST anomalies are proximal, with their tropical footprints offering potential mechanisms for their influence. In contrast, the PDO SST anomalies are distant and focused in the midlatitudes, disadvantaging them from the influence potential perspective, especially as only the tropical SST anomalies are generally viewed as influential on faraway regions. Interestingly, these disadvantages disappear once one recognizes that the PDO is not without tropical links: Guan and Nigam (2008) showed the PDO counterpart in their spatiotemporal analysis [called by them Pacific decadal variability–North Pacific (PDV-NP)] to be linked with the tropical Indian and Pacific basin SSTs;[1] see also Deser et al. (2004). The PDO's modest influence on Sahel rainfall, if realized through its tropical Indian Ocean footprints, would be consistent with the findings of Hagos and Cook (2008).

Secular change is often characterized using the century-long linear trends in observational records, as for the Sahara's expanse in Fig. 6. The linear trend is however susceptible to the aliasing of multidecadal variability should the latter be prominently manifest in the record, as is the case in summer (cf. Fig. 6).

[1] Figure 12 of Guan and Nigam (2008) shows SST regressions and correlations on the PDV-NP SST principal component. The correlation map readily reveals the tropical links, especially in the Indian Ocean and western Pacific where smaller amplitudes of SST variability create a detection challenge, but not for the correlation statistic.

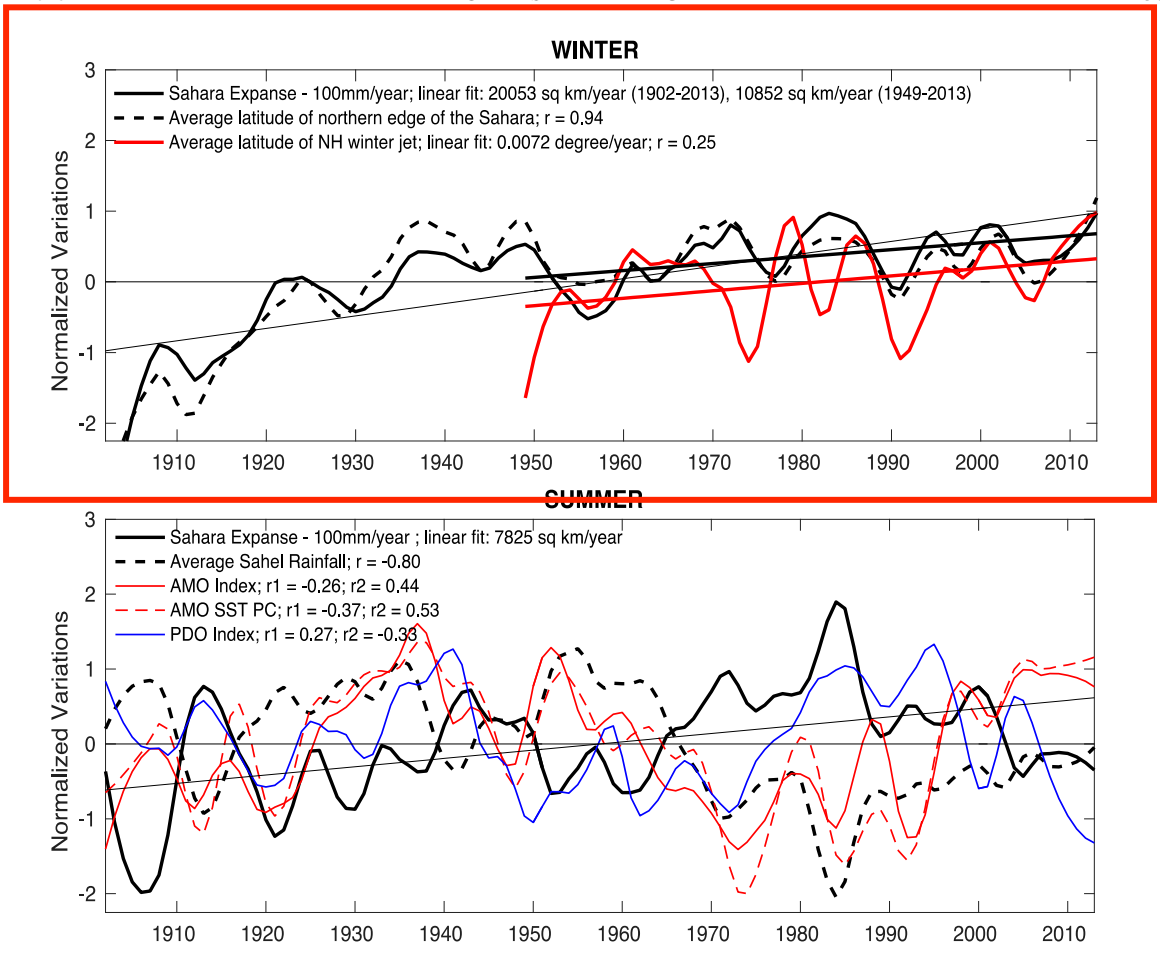

FIG. 6. The Sahara Desert's expanse during 1902–2013. The boreal (top) winter and (bottom) summer expanse is shown using the thick solid black line. The thin black straight line is the linear fit to the desert expanse over the entire period; it is the basis of the area-trend analysis reported in Table 1 (line slopes are noted in the legend). The thick black line is the linear fit to the winter desert expanse during 1949–2013—the period for which the latitude of the winter subtropical jet is plotted (solid red line, top). The Sahara expanse trend is significant at the 95% level in winter (both periods) and summer. Indices of SST and rainfall variability with potential links to the Sahara Desert's summer expanse are shown in (bottom), along with their correlation coefficients. For each index, r1 (r2) is the correlation between the index and Sahara expanse (Sahel rainfall). The AMO and PDO are displayed using their common SST indices; an SST principal component (PC)-based AMO index is also shown. The rainfall over the Sahel is plotted as well. All time series depict normalized anomalies after 10% Loess smoothing; the time series for the latitude of the Northern Hemisphere (NH) subtropical jet was smoothed with a 20% Loess function. All time series are normalized by their standard deviations; these are 703 903 km^2, 0.458 mm day^{-1}, 0.245, 1.005, 0.977, 113 9951 km^2, 1.363°, and 0.688° for the Sahara's summer expanse, the Sahel's summer rainfall, the AMO index, the AMO PC, the PDO index, the Sahara's winter expanse, the Sahara's northern latitude, and the NH winter jet latitude, respectively.

The origin of the 112-yr linear trend (referred to as the secular trend) in the Sahara's summer expanse remains to be elucidated; the elucidation is challenging, especially, for an observational analysis. Trends on centennial and longer time scales can potentially result from the interaction of multidecadal variabilities (e.g., the PDO and AMO; see Fig. 8 and discussion in section 8) and, of course, from the increasing concentration of greenhouse gases and aerosol loading (e.g., Held et al. 2005) and the related change in SST distribution (Nigam and Ruiz-Barradas 2016; see their Fig. 23.6).

7. Simulation of twentieth-century hydroclimate trends by IPCC-AR5 climate models

Climate system models contributing to the IPCC AR5 typically run in the projection mode, yielding 50–100-yr climate change projections for various greenhouse gas concentration scenarios. The very long-lead nature of

climate projections and the implicit lack of exposure of climate-change modeling to the forecast-verification cycles make model evaluation (and improvement) challenging. The few available options include assessment of the veracity of historical simulations by the same models, such as of the modeled twentieth-century secular trend in SAT for which validating observations exist. Related assessments at seasonal resolution accord additional precious evaluative opportunities—seized in this analysis—especially as the observed twentieth-century SAT trends exhibit striking seasonality over many Northern Hemisphere continents (Nigam et al. 2017). Although characterization of projected climate change over Africa is beyond the scope of this paper, an evaluation of historical simulations is important for providing weights for model projections during construction of the ensemble-averaged projection from a multitude of models that differ widely in their historical simulation capabilities.

The winter and summer simulations produced by five IPCC AR5 participant models (two U.S. and three European models) are analyzed. We chose not to analyze the entire CMIP5 model suite in the interest of an in-depth analysis of each model's simulations, including all of its ensemble members. Examining models individually is important for determining which ones will likely provide reliable hydroclimate projections. The five chosen models were developed at the leading climate modeling centers in the United States and Europe, and have been extensively analyzed and used for mitigation and adaptation planning.

The SAT and precipitation trends over the 103-yr historical simulation period (1902–2004), averaged across ensemble members from each model, are shown in Fig. 7; observed trends over the same period (i.e., the simulation target) are shown at the top of each column. The simulated SAT trends are varied and, mostly, inconsistent with the observed ones. For example, the observed trends in winter are notable over the so-called Hump of Africa—the northwestern protrusion of the continent—but none of the simulated trends, except for NCAR's, have this focus. Likewise, summer SAT trends are noteworthy over the Mediterranean rim countries of Algeria, Tunisia, and Libya but absent in the majority of analyzed simulations, with the MPI, and to some extent NCAR, being the exceptions. The austral winter warming over southern Africa, in contrast, is reasonably captured in many simulations but not by GFDL's. Finally, the robust seasonality in observed SAT trends, for example, around Lake Chad but especially to its northeast, is not captured in most simulations.

The observed and simulated twentieth-century precipitation trends are displayed in the right columns of Fig. 7. The austral summer trends consist, principally, of an east–west dipole over southern Africa, with wetting trends over the African Great Lakes. The trend structure is, to an extent, present in the NCAR simulation but in no other. The intense drying trend over tropical West Africa and the Sahel interior (the region around and to the east of Lake Chad, up to Ethiopia and Somalia) in boreal summer has no serious counterpart in the historical simulations except for NCAR's and, to an extent, GFDL's; the drying trends in other simulations are weak (in the noise range) and/or misplaced. Perhaps the historical simulations not examined in this analysis perform better as some investigators have found this simulation ensemble capable of reproducing the large-scale twentieth-century drying of the Sahel, including seasonal aspects (e.g., Biasutti 2013).

8. Concluding remarks

The footprints of climate change over the African continent are widely noted (e.g., Niang et al. 2014; WMO 2015) but even region-specific descriptions seldom stray from the annual-mean displays of hydroclimate trends—and this over the African continent, where the seasonal waxing and waning of the Sahara Desert and the complementary retraction and expansion of Sahel rainfall rule the northern continent. Southern Hemisphere Africa is also no stranger to the munificence of the seasonal cycle, which brings rainfall and life to vast stretches of the Namib–Kalahari Desert in austral summer. The utility of the seasonal perspective in climate change (i.e., seasonally stratified centennial trends in precipitation and near-surface air temperature) for long-term water resource management cannot, of course, be overstated.

The centennial SAT trends are larger over the northern continent, especially in the northwestern sector and North Africa (Algeria and Libya) where they are often greater than 1.6°C century^{-1}. The trends are furthermore pronounced in boreal summer, amplifying the regional seasonal cycle (i.e., making hot summers even hotter and exacerbating heat-related distress). Another focal point of large SAT trends over north Africa is the region to the west of the White Nile (central-southern Sudan). For context, these SAT trends are not much smaller than the largest SAT trends over North America (e.g., Nigam et al. 2017; Fig. 1) that are manifest over western-central Canada in winter.

Centennial precipitation trends, especially the drying ones, are notable over the tropical continent (i.e., in the region between the Sahara and the Namib–Kalahari deserts). River-basin-wise, impressive drying trends are found in the source region of the Niger River from spring to fall (i.e., in the local rainy seasons); the decline is impressive because it represents a 10%–25% decline

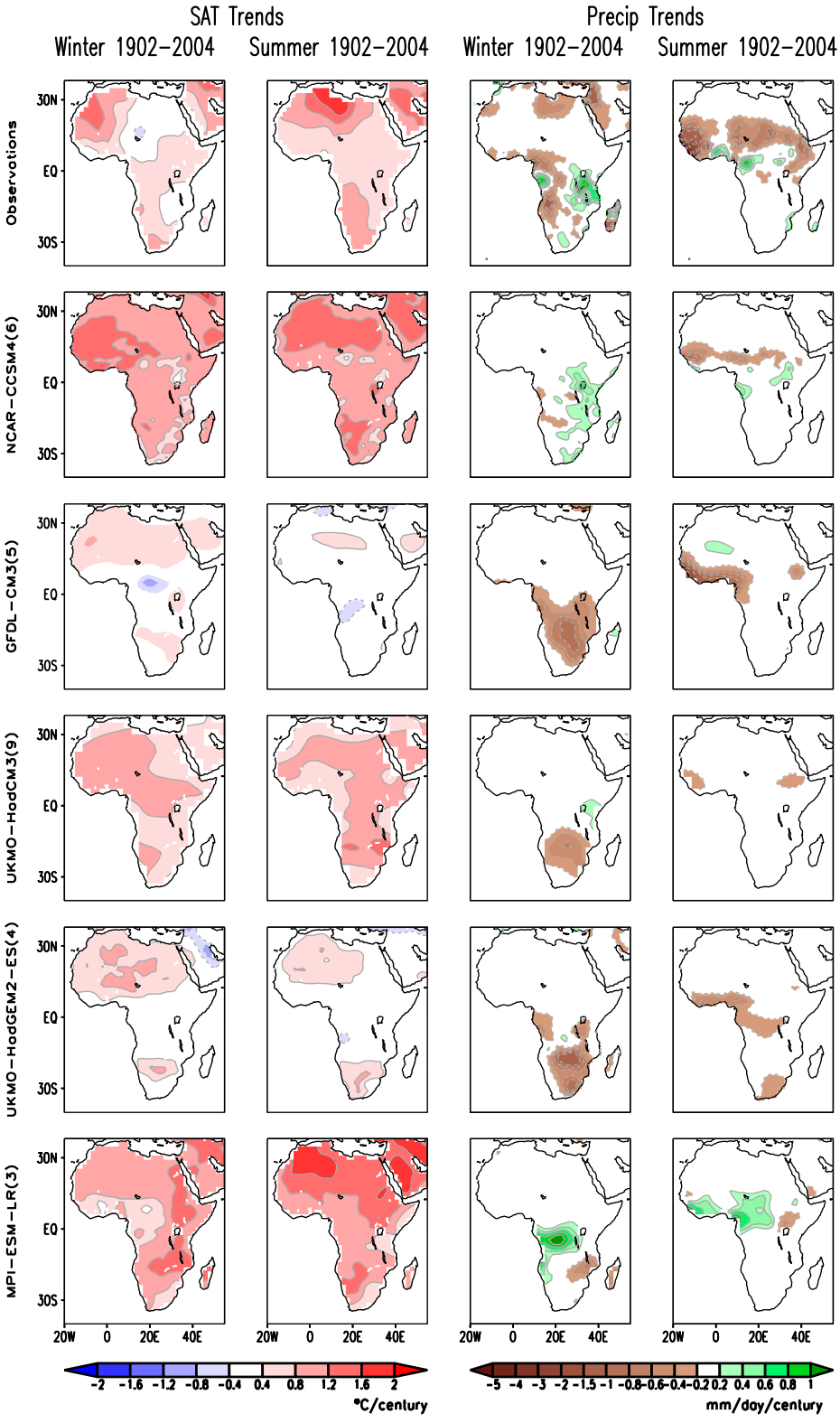

FIG. 7. The linear trend in boreal winter and summer (left) SAT and (right) precipitation averaged across all ensemble members of the model's twentieth-century (1902–2004) historical simulation produced for the IPCC AR5; simulations from five models are analyzed. (top) The observed SAT trend is the average of three independent analyses of SAT, while the observed precipitation trend is from the GPCC analysis. The number of ensemble members is indicated in parentheses next to the model's name in the *y*-axis labels on the left. Model fields are displayed after one application of smth9 in GrADS.

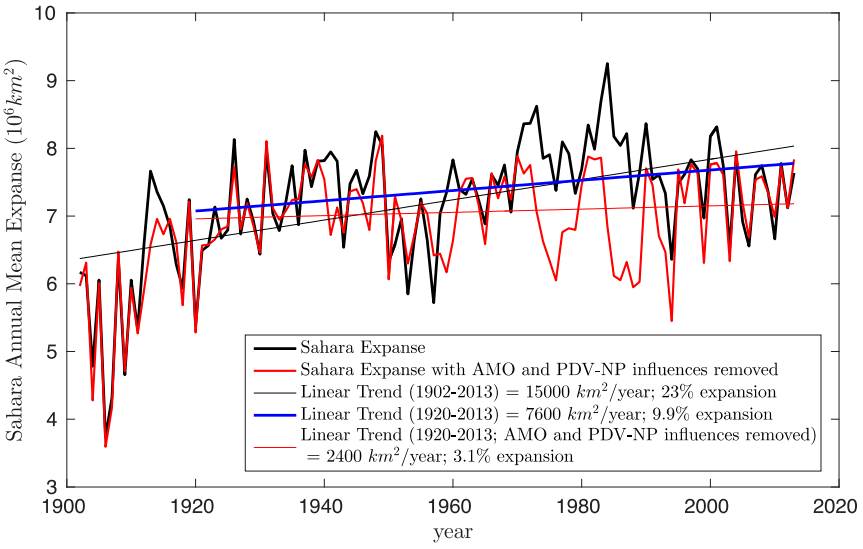

FIG. 8. Annual-mean Sahara Desert expanse (km^2; computed from the area-trend method). Linear trends are shown for 1902–2013 (thin black line) and 1920–2013 (thick blue line); the values are noted in the legend. The red curve and the corresponding 1920–2013 linear trend (thin red line) track desert expanse after removal of the AMO's and PDO's influence from the precipitation data set. The area-expansion percentages are all computed using the 1902–2013 climatological desert expanse.

in seasonal rainfall over the course of the twentieth century. Another focal point of declining rainfall is the Congo River basin, and the Blue Nile source region around Lake Tana in Ethiopia (the latter in boreal summer, the peak rainfall season).

When viewed together, the key features of the centennial drying trends can be interpreted as the southward expansion of the Sahara Desert during boreal spring to fall, or alternatively, as the equatorward retreat of the northern edge of the Sahel rainfall belt. The winter rainfall decline in northern Africa, likewise, alludes to the Sahara's northward advance. We show that the Sahara Desert has expanded significantly over the twentieth century—by 11%–18% depending on the season—using conservative estimates from the area-trend method. In winter, the desert's northward advance arises from the secular expansion of the tropics and the resulting subtropical descent (and desertification). The southward expansion in summer is linked to the SST variability in the Atlantic and Pacific basins on multidecadal time scales, through the Atlantic multidecadal oscillation's (AMO) and Pacific decadal oscillation's (PDO) impact on Sahel rainfall. On centennial time scales, the summer expansion is related to aliased multidecadal variabilities and the increasing concentration of greenhouse gases and aerosol loading (e.g., Held et al. 2005).

The seasonally stratified analysis of hydroclimate trends—the focus of the study—was complemented by analyses of the annual-mean trends. The latter, more directly relatable to deserts in view of the canonical annual-rainfall-based desert definition, also revealed impressive expansion rates for the Sahara Desert over the twentieth century (Table 1, Fig. 8). The rate is however sensitive to the analysis period, from exposure to the aliasing of multidecadal variability (e.g., AMO and PDO) and variability of the rain gauge network. Figure 8 plots the linear expansion rate of the Sahara Desert's annual expanse over two different multidecadal periods, both ending in 2013; the rates are quite variable, ranging from 9.9% to 23%, likely from the impact of the coarse rain gauge network in the early part of the 20th century (cf. Fig. 8).

The aliasing of multidecadal variability in the linear trend in the Sahara's annual-mean expanse is directly investigated during the relatively stable rain-gauge network period (1920 onwards) in Fig. 8. The AMO and PDO influences are removed from the precipitation record via linear regression.[2] The annual-mean Sahara

[2] The seasonally stratified precipitation fields are regressed onto the seasonal AMO and PDV-NP SST principal components (PCs, which are orthonormal; see Nigam et al. 2011) over the full period (1902–2013). The influence of these multidecadal variability modes is computed by multiplying their time-independent regression coefficients by their time-varying PC, seasonally. The influence is then subtracted from the precipitation record, and the desert expanse recomputed, as before (section 2c).

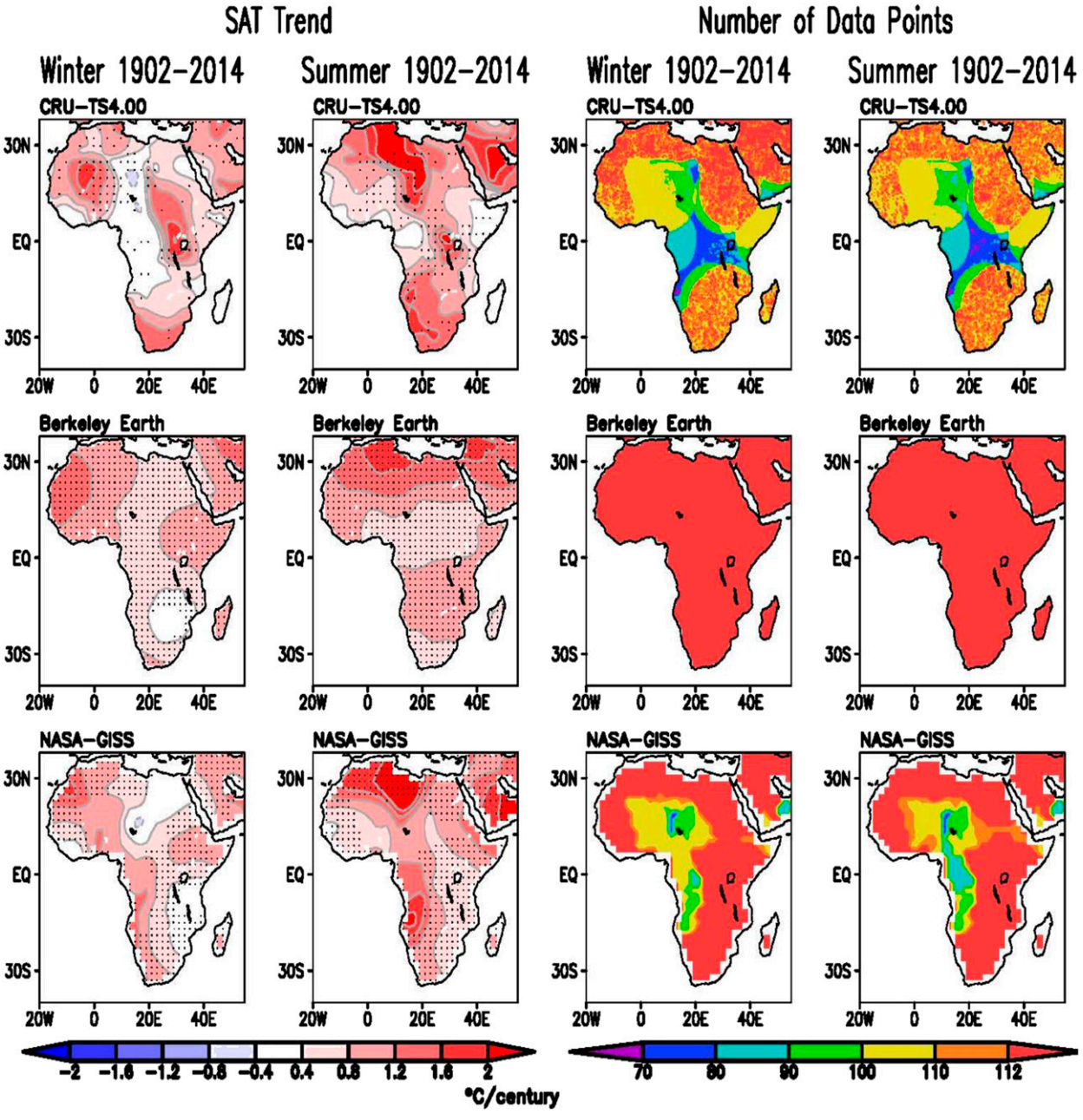

FIG. A1. (far left) Winter (DJF) and (center left) summer (JJA) linear trends in three independent analyses of observed SAT during 1902–2014: (top) the 0.5° resolution CRU TS4.00, (middle) the 1.0° resolution Berkeley Earth, and (bottom) the 2.0° resolution NASA GISS. Contour–shading interval and shading threshold is 0.5°C century^{-1}. Fields are displayed after 9, 1, and 1 application(s), respectively, of smth9 in GrADS. Trends significant at the 95% confidence level are stippled. (center right),(far right) As at left, but for the number of nonmissing data points over the 113-yr period for winter and summer, respectively.

Desert expanse sans the multidecadal modes' influence is shown in Fig. 8 by the red curve. The AMO's and PDO's influence is strong during the 1970s–90s when the red curve diverges from the black one; their contribution to the drying of the Sahel during the 1950s–80s is evident. The different linear trends of the two time series indicate that about two-thirds of the ~10% increase in the Sahara Desert's annual-mean expanse during 1920-2013 is attributable to multidecadal SST variability, and the remaining one-third to the rising greenhouse gas concentrations and aerosol loadings, and other factors.

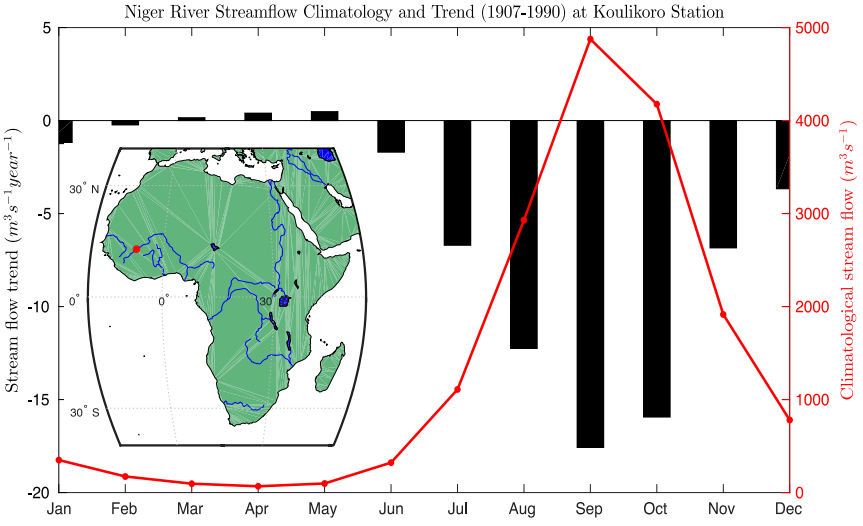

FIG. B1. Monthly streamflow climatology (red line; right axis; $m^3\ s^{-1}$) and trend (black bars; left axis; $m^3\ s^{-1}\ yr^{-1}$) for the 1907–90 period at the Koulikoro monitoring station (12.887°N, 7.54°W) in western Mali. The station location in the source region of the Niger River is shown using the red dot in the inset map.

There are other interesting features such as the increasing rainfall trends over the African Great Lakes during austral spring and summer. Are these generated from trends in regional circulation and related moisture transports (and convergence) and/or from trends in the seasonal cross-equatorial transition/position of the intertropical convergence zone (ITCZ; Waliser 2003)? The positive (negative) rainfall trends over southern (northern) equatorial Africa, including the African Great Lakes, are not inconsistent with the latter possibility. Regardless, these questions merit further analysis.

Finally, we show the twentieth-century historical simulations produced by several climate-system models whose climate projections informed the IPCC AR5 assessment in 2013 to be devoid of realistic centennial trends in regional hydroclimate over the African continent. Projections of African climate change from these models need to be interpreted with caution. The seasonal characterization of centennial trends in observed hydroclimate moreover accords an opportunity for evaluation of climate projection models by expanding the phase space for model vetting.

Characterization of the seasonal twentieth-century trends in observed and simulated hydroclimate is a necessary first step in the documentation of climate change over the African continent. A follow-on analysis to investigate the mechanisms generating the seasonality and regionality of the hydroclimate trends is clearly needed to advance the process-level understanding of the origin of these trends. The challenge is patent as observational records, especially of near-surface (e.g., 925-hPa) winds, evapotranspiration, and soil moisture are sparse over the African continent while the current IPCC-class climate system models are unable to simulate the hydroclimate trends in historical simulations, precluding the use of models in attribution analysis.

Acknowledgments. NT was supported by the Department of Defense (DoD) through the National Defense Science and Engineering Graduate Fellowship (NDSEG) Program. SN acknowledges support from the U.S. National Science Foundation through Grant AGS 1439940. The authors thank Dr. Alfredo Ruiz-Barradas for advice on datasets and help with analysis techniques. We thank the reviewers and editor Wenhong Li for their careful reading of the manuscript and for their constructive advice. The manuscript has also benefited from the feedback provided by Dr. Sharon Nicholson.

APPENDIX A

Centennial Trends in Three Analyses of SAT Observations

The observed SAT trend in the main text (e.g., Fig. 2 refers to the average trend in three independent analyses (CRU TS4.00, Berkeley Earth, and NASA GISS) of SAT observations. The trend and data density in each analysis is shown in Fig. A1 for both winter and summer. Not surprisingly, modest differences are evident on regional scales (e.g., in the strength and location of austral winter warming over southern Africa). Likewise, boreal winter warming over Sudan has varied representation, being strong in the CRU TS4.00 analysis but not in

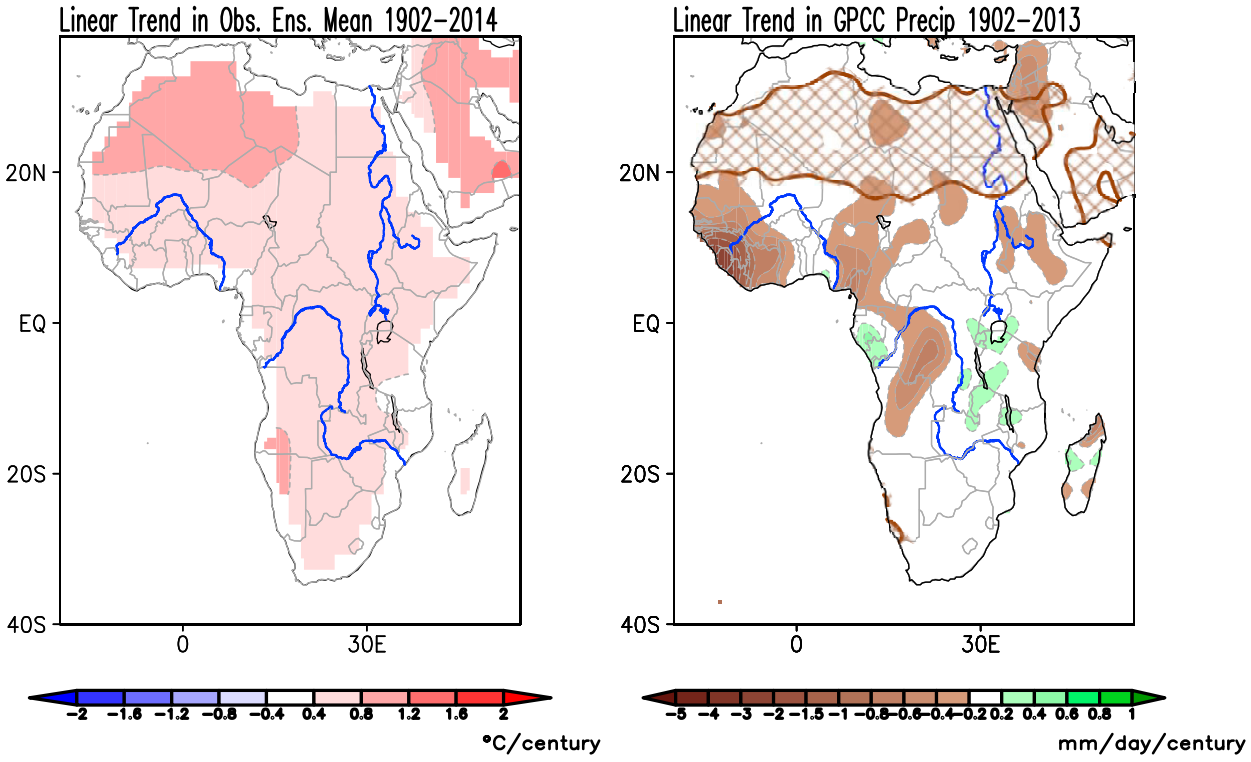

FIG. C1. Linear trend in annual-mean (left) SAT (°C century^{-1}) and (right) precipitation (mm day^{-1} century^{-1}) over the 1902–2014 period (1902–2013 for precipitation). The SAT trend is the average of the trends in three independent analyses of SAT observations (as in Fig. 2), while the precipitation one is based on the GPCC analysis (as in Fig. 3). Thick solid brown contours mark the 100 mm yr^{-1} climatological annual-mean precipitation isoline, and brown hatching indicates regions where climatological annual-mean precipitation is less than 100 mm yr^{-1}. Both datasets are at 0.5° resolution. Contour and shading interval is 0.4°C century^{-1} for SAT and as indicated by the brown–green color bar for precipitation. Fields are displayed after nine applications of the 9-point smoother (smth9) in GrADS. Major rivers are shown in thin blue lines and country boundaries in thin gray lines.

others. Some of these differences, undoubtedly, arise from the spatiotemporal sparseness of the CRU and NASA GISS datasets. A broader view, however, indicates consistency on the larger scales among the three trends, with the common features manifest in the average trend and in its discussion (section 4).

APPENDIX B

Niger River Streamflow Climatology and Trends

The strong centennial decline in seasonal precipitation over the source region of the Niger River (Fig. 3) must impact its streamflow. Figure B1 shows the monthly streamflow climatology (red line) and trends (black bars) over the 1907–90 period at a monitoring station in the source region. Climatological streamflow is weakest in spring even though regional precipitation is not a minimum in this season (Fig. 1), in part because spring rainfall is effectively used in recharging soil moisture after the dry season (boreal winter). Even otherwise, a 1–2-month lag of streamflow vis-à-vis regional precipitation is not uncommon because of the aggregation and drainage delays generated in large watersheds, and the temporal phasing of other surface water losses (e.g., evapotranspiration). The streamflow peaks in September, following the wet season (June–August; Fig. 1), again with some delay. It is thus not surprising that the streamflow trend is most negative in fall—that is, following the season of most negative precipitation trends (summer, Fig. 3).

The decline in Niger River's source region streamflow in September is very steep: A 15 m^3 s^{-1} yearly decrease, or a 1500 m^3 s^{-1} centennial decrease where the climatological flow is ~5000 m^3 s^{-1}, represents a 30% reduction over the twentieth century.

APPENDIX C

Annual SAT and Precipitation Trends

Figure C1 displays the linear trends in annual SAT and precipitation over Africa. A comparison with seasonal

trends (Figs. 2 and 3) illustrates the advantage of the seasonal perspective adopted in the main text. While annual-mean trends clarify the regions of greatest warming and drying on the continent, they can mask notable subannual (i.e., interseasonal) variations in trends that can modulate the regional seasonal cycle: For example, Fig. C1 shows maximum annual SAT trends over Sudan and northern Africa but the amplification of the seasonal cycle and related intensification of heat distress is only ascertainable from the structure of seasonal trends, as discussed in section 4. The annual perspective can sometimes be misleading as well, as in the case of precipitation trends over Kenya/Tanzania (Fig. 3), which are notable in most seasons but offsetting, leading to an annual-mean trend of close to zero. The impact on agriculture, however, need not be negligible as it is sensitive primarily to the growing seasons' trends.

REFERENCES

Archer, C. L., and K. Caldeira, 2008: Historical trends in the jet streams. *Geophys. Res. Lett.*, **35**, L08803, https://doi.org/10.1029/2008GL033614.

Becker, A., P. Finger, A. Meyer-Christoffer, B. Rudolf, K. Schamm, U. Schneider, and M. Ziese, 2013: A description of the global land-surface precipitation data products of the Global Precipitation Climatology Centre with sample applications including centennial (trend) analysis from 1901–present. *Earth Syst. Sci. Data*, **5**, 71–99, https://doi.org/10.5194/essd-5-71-2013.

Biasutti, M., 2013: Forced Sahel rainfall trends in the CMIP5 archive. *J. Geophys. Res. Atmos.*, **118**, 1613–1623, https://doi.org/10.1002/jgrd.50206.

——, and A. Giannini, 2006: Robust Sahel drying in response to late 20th century forcings. *Geophys. Res. Lett.*, **33**, L11706, https://doi.org/10.1029/2006GL026067.

Breman, H., and C. T. de Wit, 1983: Rangeland productivity and exploitation in the Sahel. *Science*, **221**, 1341–1347, https://doi.org/10.1126/science.221.4618.1341.

Busby, J. W., K. H. Cook, E. K. Vizy, T. G. Smith, and M. Bekalo, 2014: Identifying hot spots of security vulnerability associated with climate change in Africa. *Climatic Change*, **124**, 717–731, https://doi.org/10.1007/s10584-014-1142-z.

Charney, J. G., 1975: Dynamics of deserts and drought in the Sahel. *Quart. J. Roy. Meteor. Soc.*, **101**, 193–202, https://doi.org/10.1002/qj.49710142802.

Chou, C., J. C. H. Chiang, C.-W. Lan, C.-H. Chung, Y.-C. Liao, and C.-J. Lee, 2013: Increase in the range between wet and dry season precipitation. *Nat. Geosci.*, **6**, 263–267, https://doi.org/10.1038/ngeo1744.

Collins, J. M., 2011: Temperature variability over Africa. *J. Climate*, **24**, 3649–3666, https://doi.org/10.1175/2011JCLI3753.1.

Cook, K. H., and E. K. Vizy, 2015: Detection and analysis of an amplified warming of the Sahara Desert. *J. Climate*, **28**, 6560–6580, https://doi.org/10.1175/JCLI-D-14-00230.1.

Dai, A., and K. E. Trenberth, 2003: New estimates of continental discharge and oceanic freshwater transport. *Symp. on Observing and Understanding the Variability of Water in Weather and Climate*, Long Beach, CA, Amer. Meteor. Soc., 11.3, https://ams.confex.com/ams/7ICSHMO/techprogram/paper_59417.htm.

Deser, C., A. S. Phillips, and J. W. Hurrell, 2004: Pacific interdecadal climate variability: Linkages between the tropics and the North Pacific during boreal winter since 1900. *J. Climate*, **17**, 3109–3124, https://doi.org/10.1175/1520-0442(2004)017<3109:PICVLB>2.0.CO;2.

Dong, B., and R. Sutton, 2015: Dominant role of greenhouse-gas forcing in the recovery of Sahel rainfall. *Nat. Climate Change*, **5**, 757–760, https://doi.org/10.1038/nclimate2664.

Ebisuzaki, W., 1997: A method to estimate the statistical significance of a correlation when the data are serially correlated. *J. Climate*, **10**, 2147–2153, https://doi.org/10.1175/1520-0442(1997)010<2147:AMTETS>2.0.CO;2.

Enfield, D. B., A. M. Mestas-Nuñez, and P. J. Trimble, 2001: The Atlantic multidecadal oscillation and its relation to rainfall and river flows in the continental U.S. *Geophys. Res. Lett.*, **28**, 2077–2080, https://doi.org/10.1029/2000GL012745.

Evan, A. T., C. Flamant, M. Gaetani, and F. Guichard, 2016: The past, present and future of African dust. *Nature*, **531**, 493–495, https://doi.org/10.1038/nature17149.

Feng, X., A. Porporato, and I. Rodriguez-Iturbe, 2013: Changes in rainfall seasonality in the tropics. *Nat. Climate Change*, **3**, 811–815, https://doi.org/10.1038/nclimate1907.

Fields, S., 2005: Continental divide: Why Africa's climate change burden is greater. *Environ. Health Perspect.*, **113**, A534–A537, https://doi.org/10.1289/ehp.113-a534.

Folland, C. K., T. N. Palmer, and D. E. Parker, 1986: Sahel rainfall and worldwide sea temperatures, 1901–85. *Nature*, **320**, 602–607, https://doi.org/10.1038/320602a0.

Giannini, A., R. Saravanan, and P. Chang, 2003: Oceanic forcing of Sahel rainfall on interannual to interdecadal time scales. *Science*, **302**, 1027–1030, https://doi.org/10.1126/science.1089357.

Guan, B., and S. Nigam, 2008: Pacific sea surface temperatures in the twentieth century: An evolution-centric analysis of variability and trend. *J. Climate*, **21**, 2790–2809, https://doi.org/10.1175/2007JCLI2076.1.

——, and ——, 2009: Analysis of Atlantic SST variability factoring interbasin links and the secular trend: Clarified structure of the Atlantic multidecadal oscillation. *J. Climate*, **22**, 4228–4240, https://doi.org/10.1175/2009JCLI2921.1.

Hagos, S. M., and K. H. Cook, 2008: Ocean warming and late-twentieth-century Sahel drought and recovery. *J. Climate*, **21**, 3797–3814, https://doi.org/10.1175/2008JCLI2055.1.

Hansen, J., R. Ruedy, M. Sato, and K. Lo, 2010: Global surface temperature change. *Rev. Geophys.*, **48**, RG4004, https://doi.org/10.1029/2010RG000345.

Harris, I., P. D. Jones, T. J. Osborn, and D. H. Lister, 2014: Updated high-resolution grids of monthly climatic observations—The CRU TS3.10 dataset. *Int. J. Climatol.*, **34**, 623–642, https://doi.org/10.1002/joc.3711.

Held, I. M., T. L. Delworth, J. Lu, K. L. Findell, and T. R. Knutson, 2005: Simulation of Sahel drought in the 20th and 21st centuries. *Proc. Natl. Acad. Sci. USA*, **102**, 17 891–17 896, https://doi.org/10.1073/pnas.0509057102.

Hoerling, M., J. Hurrell, J. Eischeid, and A. Phillips, 2006: Detection and attribution of twentieth-century northern and southern African rainfall change. *J. Climate*, **19**, 3989–4008, https://doi.org/10.1175/JCLI3842.1.

Hulme, M., R. Doherty, T. Ngara, M. New, and D. Lister, 2001: African climate change: 1900-2100. *Climate Res.*, **17**, 145–168, https://doi.org/10.3354/cr017145.

James, I. N., 2003: Hadley circulation. *Encyclopedia of Atmospheric Sciences*, J. R. Holton et al., Eds., Elsevier, 919–929.

Kalnay, E., and Coauthors, 1996: The NCEP/NCAR 40-Year Reanalysis Project. *Bull. Amer. Meteor. Soc.*, **77**, 437–471, https://doi.org/10.1175/1520-0477(1996)077<0437:TNYRP>2.0.CO;2.

Kavvada, A., A. Ruiz-Barradas, and S. Nigam, 2013: AMO's structure and climate footprint in observations and IPCC AR5 climate simulations. *Climate Dyn.*, **41**, 1345–1364, https://doi.org/10.1007/s00382-013-1712-1.

Knight, J. R., C. K. Folland, and A. A. Scaife, 2006: Climate impacts of the Atlantic multidecadal oscillation. *Geophys. Res. Lett.*, **33**, L17706, https://doi.org/10.1029/2006GL026242.

Linkin, M. E., and S. Nigam, 2008: The North Pacific Oscillation–west Pacific teleconnection pattern: Mature-phase structure and winter impacts. *J. Climate*, **21**, 1979–1997, https://doi.org/10.1175/2007JCLI2048.1.

Maidment, R. I., R. P. Allan, and E. Black, 2015: Recent observed and simulated changes in precipitation over Africa. *Geophys. Res. Lett.*, **42**, 8155–8164, https://doi.org/10.1002/2015GL065765.

Mantua, N. J., S. R. Hare, Y. Zhang, J. M. Wallace, and R. Francis, 1997: A Pacific interdecadal climate oscillation with impacts on salmon production. *Bull. Amer. Meteor. Soc.*, **78**, 1069–1079, https://doi.org/10.1175/1520-0477(1997)078<1069:APICOW>2.0.CO;2.

Martin, E. R., and C. D. Thorncroft, 2014: The impact of the AMO on the West African monsoon annual cycle. *Quart. J. Roy. Meteor. Soc.*, **140**, 31–46, https://doi.org/10.1002/qj.2107.

Mohino, E., S. Janicot, and J. Bader, 2011: Sahel rainfall and decadal to multi-decadal sea surface temperature variability. *Climate Dyn.*, **37**, 419–440, https://doi.org/10.1007/s00382-010-0867-2.

Niang, I., and Coauthors, 2014: Africa. *Climate Change 2014: Impacts, Adaptation, and Vulnerability. Part B: Regional Aspects*. V. R. Barros, et al., Eds., Cambridge University Press, 1199–1265.

Nicholson, S. E., 2000: Land surface processes and Sahel climate. *Rev. Geophys.*, **38**, 117–139, https://doi.org/10.1029/1999RG900014.

——, 2001: Climatic and environmental change in Africa during the last two centuries. *Climate Res.*, **17**, 123–144, https://doi.org/10.3354/cr017123.

——, and J. Kim, 1997: The relationship of the El Nino–Southern Oscillation to African rainfall. *Int. J. Climatol.*, **17**, 117–135, https://doi.org/10.1002/(SICI)1097-0088(199702)17:2<117::AID-JOC84>3.0.CO;2-O.

Nigam, S., and S. C. Chan, 2009: On the summertime strengthening of the Northern Hemisphere Pacific sea level pressure anticyclone. *J. Climate*, **22**, 1174–1192, https://doi.org/10.1175/2008JCLI2322.1.

——, and A. Ruiz-Barradas, 2016: Key role of the Atlantic multidecadal oscillation in twentieth century drought and wet periods over the US Great Plains and the Sahel. *Dynamics and Predictability of Large-Scale, High-Impact Weather and Climate Events*, J. Li et al., Eds., Cambridge University Press, 255–270.

——, B. Guan, and A. Ruiz-Barradas, 2011: Key role of the Atlantic Multidecadal Oscillation in 20th century drought and wet periods over the Great Plains. *Geophys. Res. Lett.*, **38**, L16713, https://doi.org/10.1029/2011GL048650.

——, N. Thomas, A. Ruiz-Barradas, and S. Weaver, 2017: Striking seasonality in the secular warming of the northern continents: Structure and mechanisms. *J. Climate*, **30**, 6521–6541, https://doi.org/10.1175/JCLI-D-16-0757.

Omondi, P., L. A. Ogallo, R. Anyah, J. M. Muthama, and J. Ininda, 2013: Linkages between global sea surface temperatures and decadal rainfall variability over Eastern Africa region. *Int. J. Climatol.*, **33**, 2082–2104, https://doi.org/10.1002/joc.3578.

Philander, S. G., 1990: *El Niño, La Niña, and the Southern Oscillation*. Academic Press, 293 pp.

Rayner, N. A., D. E. Parker, E. B. Horton, C. K. Folland, L. V. Alexander, D. P. Rowell, E. C. Kent, and A. Kaplan, 2003: Global analyses of sea surface temperature, sea ice, and night marine air temperature since the late nineteenth century. *J. Geophys. Res.*, **108**, 4407, https://doi.org/10.1029/2002JD002670.

Rohde, R., and Coauthors, 2013: Berkeley Earth temperature averaging process. *Geoinfor Geostat: An Overview*, **1** (3), 1–13.

Rowell, D. P., B. B. B. Booth, S. E. Nicholson, and P. Good, 2015: Reconciling past and future rainfall trends over East Africa. *J. Climate*, **28**, 9768–9788, https://doi.org/10.1175/JCLI-D-15-0140.1.

Santer, B. D., T. M. L. Wigley, J. S. Boyle, D. J. Gaffen, J. J. Hnilo, D. Nychka, D. E. Parker, and K. E. Taylor, 2000: Statistical significance of trends and trend differences in layer-average atmospheric temperature time series. *J. Geophys. Res.*, **105**, 7337–7356, https://doi.org/10.1029/1999JD901105.

Schlesinger, M. E., and N. Ramankutty, 1994: An oscillation in the global climate system of period 65–70 years. *Nature*, **367**, 723–726, https://doi.org/10.1038/367723a0.

Schneider, U., and Coauthors, 2014: GPCC's new land surface precipitation climatology based on quality-controlled in situ data and its role in quantifying the global water cycle. *Theor. Appl. Climatol.*, **115**, 15–40, https://doi.org/10.1007/s00704-013-0860-x.

Schreck, C. J., and F. H. M. Semazzi, 2004: Variability of the recent climate of eastern Africa. *Int. J. Climatol.*, **24**, 681–701, https://doi.org/10.1002/joc.1019.

Seidel, D. J., Q. Fu, W. J. Randel, and T. J. Reichler, 2008: Widening of the tropical belt in a changing climate. *Nat. Geosci.*, **1**, 21–24, https://doi.org/10.1038/ngeo.2007.38.

Taylor, K. E., R. J. Stouffer, and G. A. Meehl, 2012: An overview of CMIP5 and the experiment design. *Bull. Amer. Meteor. Soc.*, **93**, 485–498, https://doi.org/10.1175/BAMS-D-11-00094.1.

Tucker, C. J., and S. E. Nicholson, 1999: Variations in the size of the Sahara Desert from 1980 to 1997. *Ambio*, **28**, 587–591.

——, H. E. Dregne, and W. W. Newcomb, 1991: Expansion and contraction of the Sahara Desert from 1980 to 1990. *Science*, **253**, 299–301, https://doi.org/10.1126/science.253.5017.299.

Villamayor, J., and E. Mohino, 2015: Robust Sahel drought due to the Interdecadal Pacific Oscillation in CMIP5 simulations. *Geophys. Res. Lett.*, **42**, 1214–1222, https://doi.org/10.1002/2014GL062473.

Vizy, E. K., and K. H. Cook, 2017: Seasonality of the observed amplified Sahara warming trend and implications for Sahel rainfall. *J. Climate*, **30**, 3073–3094, https://doi.org/10.1175/JCLI-D-16-0687.1.

Waliser, D. E., 2003: Intertropical convergence zone. *Encyclopedia of Atmospheric Sciences*, J. R. Holon et al., Eds., Elsevier, 2325–2334.

Weare, B. C., and J. S. Nasstrom, 1982: Examples of extended empirical orthogonal function analyses. *Mon. Wea. Rev.*, **110**, 481–485, https://doi.org/10.1175/1520-0493(1982)110<0481:EOEEOF>2.0.CO;2.

Williams, A. P., and C. Funk, 2011: A westward extension of the warm pool leads to a westward extension of the Walker circulation, drying eastern Africa. *Climate Dyn.*, **37**, 2417–2435, https://doi.org/10.1007/s00382-010-0984-y.

Willmott, C. J., and K. Matsuura, 2015: Terrestrial precipitation: 1900–2014 gridded monthly time series (1900–2014). Version 4.01, http://climate.geog.udel.edu/~climate/html_pages/Global2014/README.GlobalTsP2014.html.

WMO, 2015: The climate in Africa: 2013. WMO-No. 1147, World Meteorological Organization, 32 pp.

Zhang, R., and T. L. Delworth, 2006: Impact of Atlantic multidecadal oscillations on India/Sahel rainfall and Atlantic hurricanes. *Geophys. Res. Lett.*, **33**, L17712, https://doi.org/10.1029/2006GL026267.

Zhang, Y., J. M. Wallace, and D. S. Battisti, 1997: ENSO-like interdecadal variability: 1900–93. *J. Climate*, **10**, 1004–1020, https://doi.org/10.1175/1520-0442(1997)010<1004:ELIV>2.0.CO;2.

Zhou, L., 2016: Desert amplification in a warming climate. *Sci. Rep.*, **6**, 31 065, https://doi.org/10.1038/srep31065.

Figure from the NSF and UMD Press Release on 29 March 2018

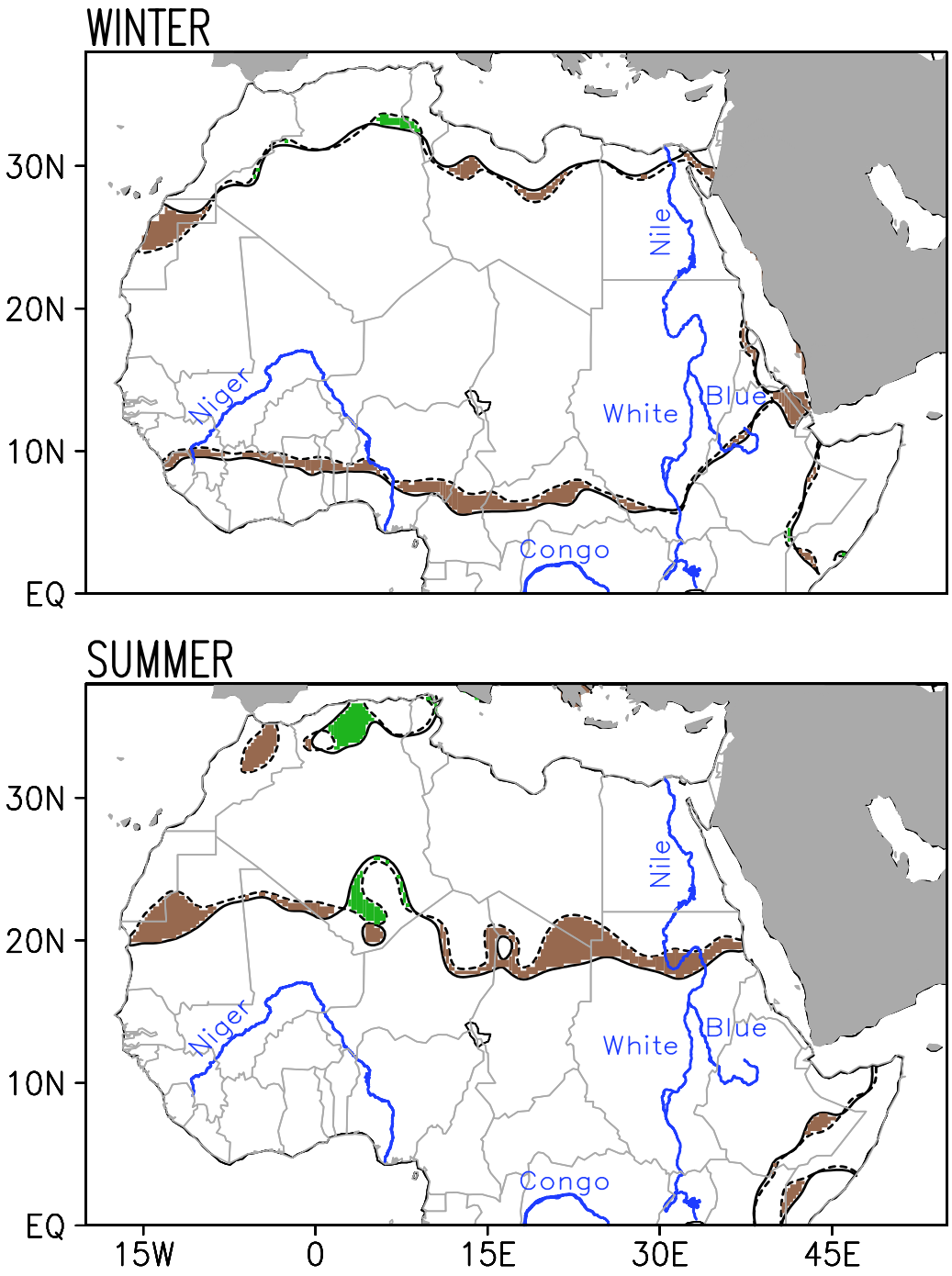

The two images show the change in the boundaries of the Sahara Desert during the period 1920-2013, broken down by season. Dotted lines show the boundary as it existed in 1920, while solid lines show the boundary in 2013; both boundaries are averaged across the three months of each season. (Winter = Dec-Feb; Summer = Jun-Aug). Brown shaded regions indicate desert advance while green shaded regions indicate desert retreat.

The seasonal analysis in Table-1 of the paper is for the 1902-2013 period. A slightly shorter period – one excluding the first two decades of the 20th century – is analyzed in Table-1a below in order to focus on the relatively stable rain gauge network period.

TABLE-1a: Expansion of the Sahara Desert seasonally during **1920-2013**, based on the movement of the 100 and 150 mm/year precipitation isolines. The expansion is computed using both area-trend and the endpoint methods; endpoint values are in parentheses. Both methods are described in section 2. The areal values are rounded off to the nearest 1000 km^2 (which is about 1/3 of the 0.5° grid cell area at the equator). DJF refers to boreal winter months (December, January, and February), and so on. The impacted countries are identifiable only from the endpoint method.

	Threshold (mm/year)	**Winter** (DJF)	**Spring** (MAM)	**Summer** (JJA)	**Fall** (SON)
Climatological Sahara extent (km^2)	**100**	14,005,000 (13,049,000)	10,697,000 (10,091,000)	7,800,000 (6,458,000)	7,744,000 (6,483,000)
	150	14,818,000 (13,965,000)	11,528,000 (10,823,000)	8,560,000 (7,544,000)	8,859,000 (8,145,000)
Sahara Expansion (km^2)	**100**	820,000 (851,000)	658,000 (653,000)	657,000 (1,017,000)	754,000 (1,165,000)
	150	630,000 (736,000)	628,000 (487,000)	669,000 (818,000)	521,000 (691,000)
Sahara Expansion (% of climatological area)	**100**	5.9% (6.5%)	6.2% (6.5%)	8.4% (15.7%)	9.7% (18.0%)
	150	5.5% (5.3%)	5.4% (4.5%)	7.8% (10.8%)	5.9% (8.5%)
Countries Affected		Egypt, Libya, Western Sahara, South Sudan, Central African Republic, Cameroon, Nigeria, Benin, Togo, Ghana, Cote D'Ivoire, Guinea	Algeria, Sudan, Chad, Nigeria, Niger, Mali	Morocco, Western Sahara, Mali, Mauritania, Algeria, Niger, Chad, Sudan	Libya, Mauritania, Western Sahara, Sudan, Chad